Msc thesis in Biomedical Engineering

Quantitative evaluation of flow inside an Organ-on-Chip model using optical coherence tomography

Devrim Tugberk
2023

TU Delft

Master of Science - Biomedical Engineering

Quantitative evaluation of flow inside an Organ-on-Chip model using optical coherence tomography

Devrim Tugberk

December 2023

A thesis submitted to the Delft University of Technology in partial fulfillment of the requirements for the degree Master of Science in Biomedical Engineering

Devrim Tugberk: *Quantitative evaluation of flow inside an Organ-on-Chip model using optical coherence tomography* (2023)

The work in this thesis was achieved through a collaboration between TU Delft and BIOND Solutions:

Mechanical, Maritime and Materials engineering
Delft University of Technology

Imaging Physics of Applied Sciences
Delft University of Technology

BIOND Solutions

Supervisors:	Jeroen Kalkman	Readers:	Jeroen Kalkman
	Kote Cheishvili		Massimo Mastrangeli
	Peter Speets		Paola Fanzio
	Anish Ballal		

Abstract

Organ-on-chip (OoC) systems combine the advantages of well-characterised human cells with the benefits of engineered, physiological-like microenvironments. The extracellular matrix is the natural microenvironment of cells in the human body responsible for providing the appropriate stimuli to cells to control cell processes such as morphogenesis. OoCs can mimic the ECM, via biomaterials, fluid channels and porous membranes, to provide the cells with (patho)physiological stimuli governed by the fluid dynamics in the system. Resolving fluid behaviour in OoC systems can not only aid in fine tuning the stimuli sensed by the cultured cells and control cell fate, but also perform quantitative OoC system inspections. The current state-of-the-art methods for evaluating fluid flow in the OoC systems are simulations, theoretical calculations, and empirical observations, however a real-time quantitative characterization is lacking. In this study, we use optical coherence tomography (OCT) for measuring both the flow in different regions of the Bi/ond inCHIPit™ microfluidic OoC and also simultaneously obtain structural information of the OoC system. We used a commercially available high resolution (3 µm in air) spectral domain OCT system. We made quantitative 1D and 2D flow measurements using phase-resolved Doppler-OCT and number fluctuation dynamic light scattering OCT to measure the flow under realistic use scenarios in the supply flow channels and, in the tissue supporting culture well where perfusion flow occurs. The results were compared to computational fluid dynamic simulations, and found to be in partial agreement. Moreover, we investigated the effects of fixed cells on the flow behaviour demonstrating real-time biologically relevant flow information and extended the work to qualitatively evaluate the perfusion flow in the presence of a liver sample in the culture well. The results of the study pave the way for further studies that determine the shear stress forces experienced by the cells in the OoC system.

Acknowledgements

At the beginning of this project in October 2022, I was told that this project has been attempted before but the desired results were not generated because of technical limitations. It was a big unknown whether the goals set for the project were achievable and this was intimidating for me. This fact, combined with knowing that I lack background knowledge on the concepts necessary for the project, I was very skeptical and intimidated. Regardless, my enthusiasm for Organs-on-Chip and the idea of collaborating with a young, energetic start-up company and contributing to their work helped me commit. Looking back, I can't refrain from smiling. I am glad I committed and grateful for all the support I had.

First, I would like to thank my TU Delft supervisor professor Jeroen. He always responded to my enthusiasm with positivity and support. We spent hours discussing not only physics, but also how to place this project within the scientific community. Despite his busy schedule, he's always made the time to discuss anything I needed to discuss. I would also like to thank Peter for spending so many hours on discussing theory, experimental ideas, and coding. I'd like to believe him and I had a unique enthusiasm for the project since he had also run this project two years ago himself. His witty humor made stressful times so much more manageable. Three quarters into the project, I got the opportunity to work with Kote. The OCT technique he developed was pivotal for this project and he showed so much support helping me apply his technique to this project and I thank him for that.

Next, I would like to thank the entire Bi/ond team, starting off with my supervisor Anish. Anish witnessed majority of 'behind the scene' moments and my frustrations with experimental challenges. He was always so patient, positive, supportive, grounding, and available. From the microfabrication side, Tawab never hesitated to show support and his enthusiasm towards the project was motivating. We spent a lot of time trying to make sense of the experimental observations and I can say the same for Lucas when it comes to operating and optimizing the micropump, a vital component of all the experiments. Last but not least, I would like to thank the biology team for helping me further extend the work and make it biologically relevant. It was truly a collaboration.

Last but definitely not the least, I would like to thank my parents, my uncle and aunt in England, and all my other family members. My close ones know that the past year and a half was the most difficult times for my parents. Despite such times they never stopped supporting, motivating, and believing in me. We kept each other mentally nourished and showed resistance, determination, and perseverance. They are my first teachers, they helped me stay on my path and I know they will continue to do so everyday.

Contents

Acronyms

1. Introduction

1.1. Conventional Drug Development

Currently, conventional drug development methods face long processing times and high failure rates due to the lack of human-relevant preclinical models with robust transferable data to human applications [49] [5]. The development of a new drug takes around 13.5 years on average, costs $2.5 billion in funding and despite all the effort 92% of the drugs fail and never make it to the market (Figure 1.1) [26]. The biggest contributing bottleneck to this problem comes from the preclinical models used to develop drugs: 2-dimensional (2D) tissue/cell cultures and animal models. The use of animal models limits the transferability of absorption, distribution, metabolism, excretion (ADME) study results to humans due to phylogenic differences between humans and animals, resulting in unreliable pharmacokinetic/pharmacodynamic (PK/PD) parameters relevant to humans [75][12][78][57]. Despite 2D cell cultures having cells of human origin, the data obtained is only partially translatable to humans due to the absence of an extracellular matrix (ECM) complexity and (patho)physiologically relevant cues to stimulate the cells to express in-vivo-like features [5]. The dissimilarity of 2D cultures and animal models to human (patho)physiology, and the 'one drug fits all' approach (negligence of accounting for individual genetic predispositions and cultural factors during drug development) are the biggest contributors to failure at the late stage of the drug development process [41][53][20]. For example, only 1 in 50 patients benefit from taking statins to lower cholesterol and there are some drugs out on the market that could be harmful to certain ethnic groups due to clinical trial participants being limited to the Western culture population [57] [20]. In addition, animal models are not only unrepresentative of human in-vitro models but their use also creates ethical dilemmas raising questions on whether animals should be taken out of their natural habitat for the benefit of human medicine [41]. Therefore, the conventional approach is now considered to be lacking and essentially highlights the need for enabling technologies that address the limitations of the conventional drug development pipeline. As a result, organs-on-chips are being considered as potentially revolutionary devices that can be an alternative to animal-based research and pave the road towards personalized medicine by allowing the consideration of each person's unique clinical, genetic, genomic, and environmental factors through (patho)physiologically relevant in-vitro models.

Organs-on-chips (OoCs) and microphysiological systems (MPS) have emerged in conjunction with advances in tissue (stem cell) engineering, microengineering, and (bio)material science to potentially tackle the aforementioned problems in the drug development pipeline, through robust disease and tissue modelling, and eventually aid in personalized/precision medicine (PM). As defined in the ORCHID Vision Workshop, OoCs are "fit-for-purpose microfluidic devices, containing living engineered organ substructures in a controlled microenvironment, that recapitulate one or more aspects of the organ's dynamics, functionality and (patho)physiological response in-vivo under real-time monitoring." [52]. The biological elements of OoCs originated from fundamental cell biology concepts and advanced through tissue engineering and biomaterial science, allowing the recreation and culturing of stable and precise tissue-specific models

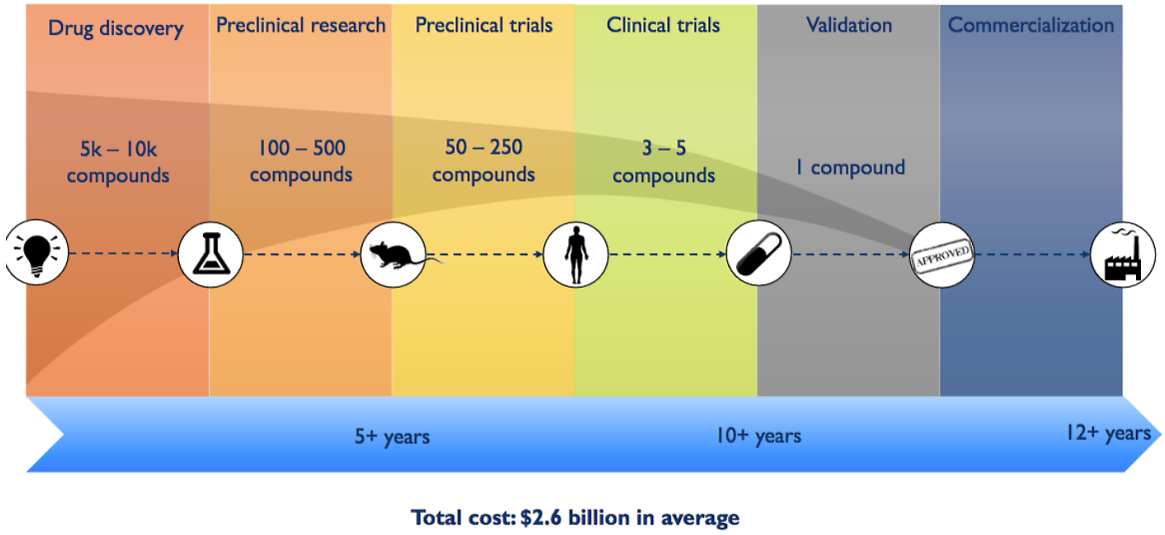

Figure 1.1.: A schematic illustrating the drug development timeline and the associated costs. Adapted from [59]

on biomaterials. Synthetic and natural biomaterials have been explored parallel to stem cell engineering, with particular interest in induced pluripotent stem cells (iPSCs) of human origin. Engineering techniques can be used to recreate the in-vivo ECM with tissue-specific properties. The use of iPSCs, in conjunction with the engineered stem cell niche, can allow researchers to have control over stem cell fate through a myriad of controllable parameters and ultimately personalize medicine [61] [74] [18]. The design and engineering elements of OoCs, such as the physicochemical cues and microarchitecture, are vital to achieving robust representations of human organs in-vitro by mimicking tissue-specific physiological-like microenvironments, and for read-outs to interpret the conditions in the OoC in real-time. The chosen fabrication methods for the OoCs should be optimized to facilitate tunable microenvironmental factors such as bioelectrical, biochemical, and biophysical cues needed to mimic the (patho)physiological microenvironment of the tissues. This means having control over tissue morphogenesis, function, microenvironment remodelling and more [61][62][36]. In addition, individual OoCs can be connected via microfluidics to create multi-organ systems, also referred to as body-on-a-chip (BoC) or human-on-a-chip (HoC) to facilitate co-culture studies and more robust in-vitro models for drug development [79] [29]. Moreover, the addition of biosensors and optical modes of analysis allow real-time on-chip readouts, and monitoring of tissue functionality and microenvironment conditions, both quantitatively and qualitatively, and carry the potential to tackle some of the technical limitations of OoCs [19] [52].

1.2. Organs-on-Chip

1.2.1. Root of Biomimicry

All cell biology processes root from and terminate in the cell nucleus – the brain of the cell where gene expressions (cell decisions) are controlled through cascades of biochemical signalling events, facilitated by specialized receptors, that get triggered or suppressed by a myriad

of genomic processes. The cell cytoskeleton is indirectly connected to the nucleus and is not only responsible for sensing mechanical cues (pressure, shear stress, stiffness, topology, curvature etc.) but also exerting forces on the cell microenvironment through mechanosensitive proteins, biochemical processes, and signalling cascades that ensure structural stability, and regulate morphogenetic movement, differentiation and homeostasis by remodelling and adapting the cytoskeleton to the new microenvironment [60]. The cell microenvironment is made up of the ECM which is a dynamic, constantly remodelling, heterogeneous component, present within all tissues and organs and is modelled based on tissue-specific needs and orchestrated by cues present in the microenvironment (ECM degrading/constructing enzymes, biochemical signals, specialized cells etc.). The ECM can provide varying, tunable mechanical cues and properties via protein fibres (e.g. different collagen types), recruitment of multiple cells into the ECM via biochemical stimuli (e.g. signalling molecules & growth factors), and alter bioelectric properties of cells present in the ECM [22]. The ECM holds a myriad of bioactive molecules and growth factors, with the ability to control their dose and availability spatiotemporally. This two-way communication between cells and their ECM has such a substantial effect on cell morphogenesis that the evolution of the metazoan and their ECM cannot be separated [45]. Ultimately, the ECM and the cell cytoskeleton co-dependently orchestrate the cascade of events that determine the type of tissue that will be created out of the group of cells, creating the basis of cell mechanotransduction and mechanobiology (Figure 1.2).

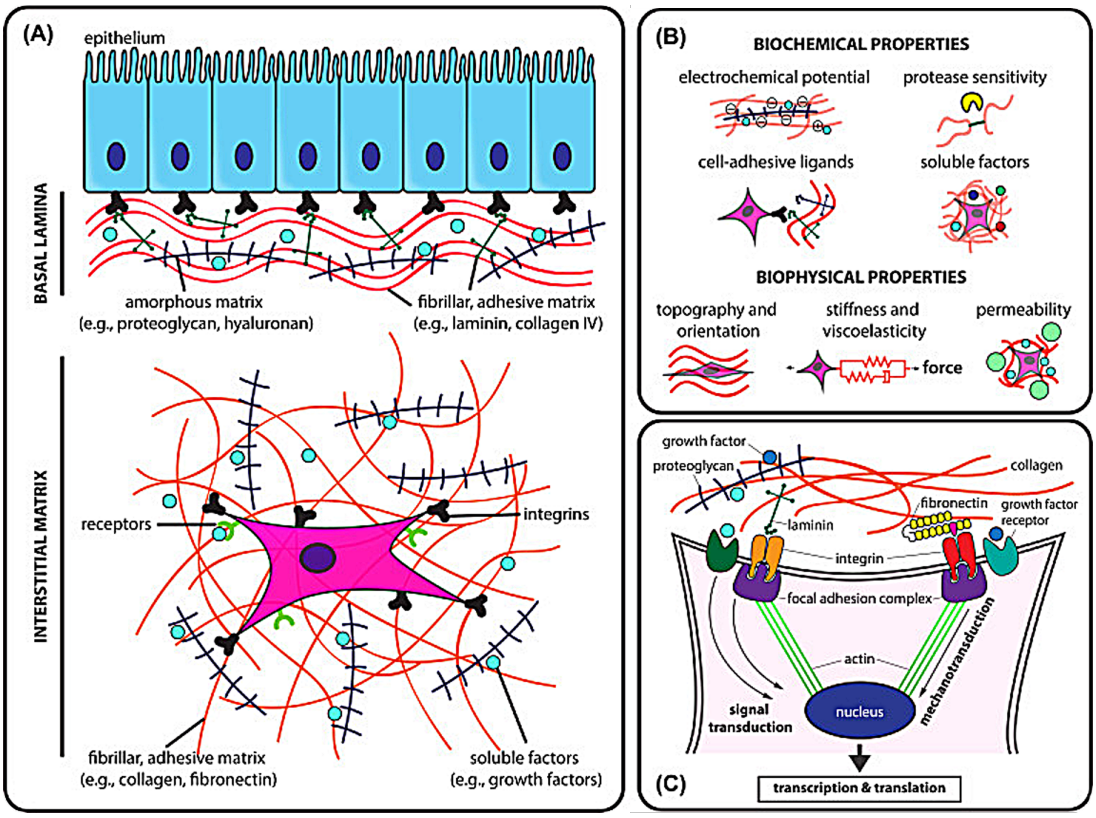

Figure 1.2.: The extracellular matrix. (A) An illustration showing the main ECM components of the basal lamina and interstitial matrix with each having slightly different functions due to different content. (B) Biophysical and biochemical properties of the ECM that directly and indirectly regulate cell behaviour. (C) The underlying mechanisms of how cell-ECM interactions occur via integrin-ECM connections. The ECM provides several cues to the cells, sensed via focal adhesions, the cytoskeleton, and receptors [37]

1.2.2. In-vitro Microenvironment

The fundamental goal of OoCs is to exploit the aforementioned cell biology concepts and engineer an in-vitro microenvironment that biomimics the in-vivo microenvironment. Identifying the key aspects of the geometrical, mechanical, and biochemical microenvironment of the tissue/organ of interest allows the reverse-engineering of the (patho)physiological microenvironment in-vitro. For now, the goal isn't to represent the entire organ but to model specific aspects of the organ via minimally functional units to study specific physiological phenomena of the functional units and applications such as drug transport, barrier function, and cellular interactions in 3D [18]. All OoCs induce a variety of physiologically-relevant cues through tissue-specific engineered microarchitectures and dynamic spatiotemporal microenvironments to ensure that the functional units of the organ model behave similarly to in-vivo conditions by expressing physiological genotypic and phenotypic characteristics. Some of these cues are induced through multi-layer membrane-based moving air-liquid interfaces to achieve mechanical stretching via vacuum deformation, flow-induced shear stress, and mass transport of nutrients, gases, and waste (Figure 1.3A), microarchitectures that provide cell guidance (Figure 1.3B), and patterned channels with porous barriers to mimic endothelial-like barriers (Figure 1.4) [82].

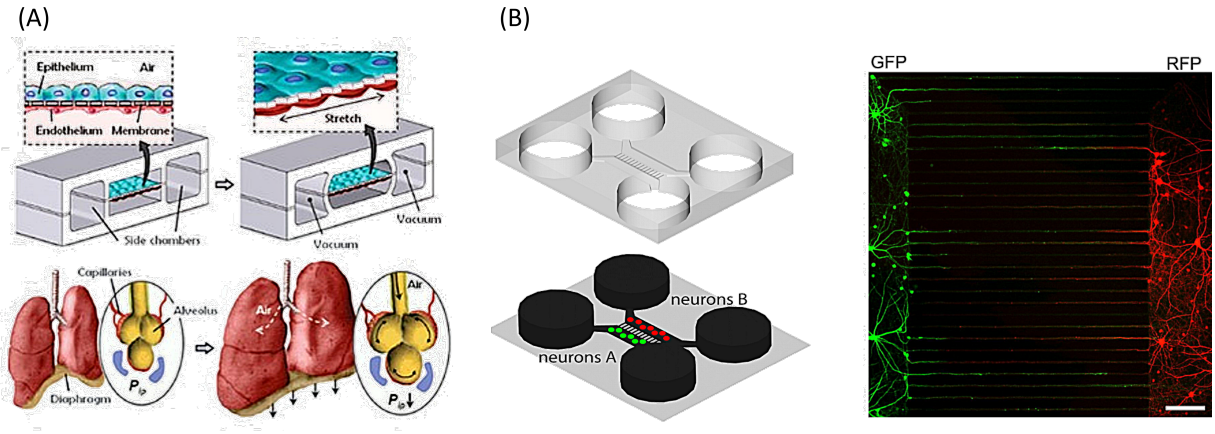

Figure 1.3.: Schematics of engineered dynamic microenvironments and microarchitectures realized in different OoCs. (A) Bioinspired alveoli-on-a-chip designed to co-culture tissue-engineered endothelial and epithelial cells and induce flow-induced shear stress and stretch to mimic the in-vivo alveolar-capillary interface [38]. (B) Differing neurons (labelled with green and red fluorescent proteins) forming dendrites due to microarchitecture guidance provided by the microgrooves of the system (scale bar = 150 µm). Modified from [71]

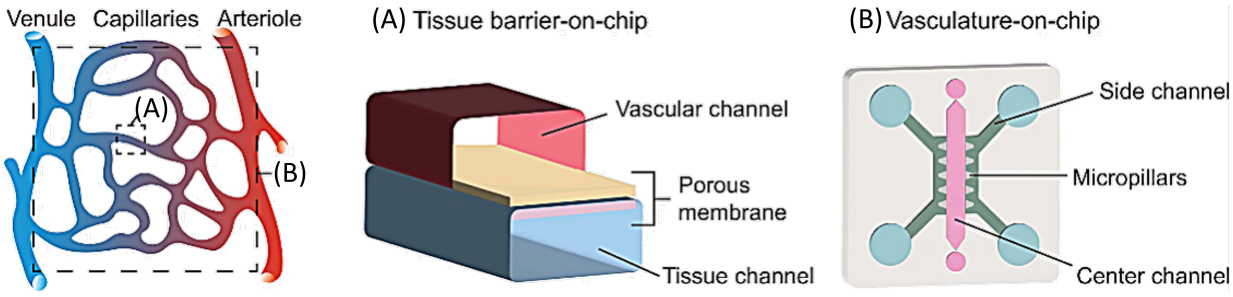

Figure 1.4.: Two different types of OoCs mimicking different regions of the native capillary complex. (A) Two microfluidic layers separated by a porous membrane. (B) 3D vascular network mimicry via parallel microchannels semi-partitioned by micropillar arrays [18]

1.2.3. OoC Limitations

Over the early years of OoCs, researchers accumulated a high volume of evidence indicating that OoCs may provide better model systems for research on health and disease compared to conventional methods. However, a significant amount of OoCs are not robust enough for all cell types, result in varying results from one user to another or even from one experiment to another, and are not yet fully compatible with already existing lab workflows of end users [54], ultimately affecting all the stakeholders involved with OoCs (Figure 1.5). In addition, there is a lack of data-supported evidence of OoCs providing actual advantages over existing conventional models or well-established approaches in tissue engineering. In conjunction, the failure of preclinical cell cultures and animal models is resulting in a decrease in the number of approved drugs. Therefore, it is no surprise that the most cited applications of OoCs come from pharmaceutical drug development processes to de-risk the current drug development pipeline [52].

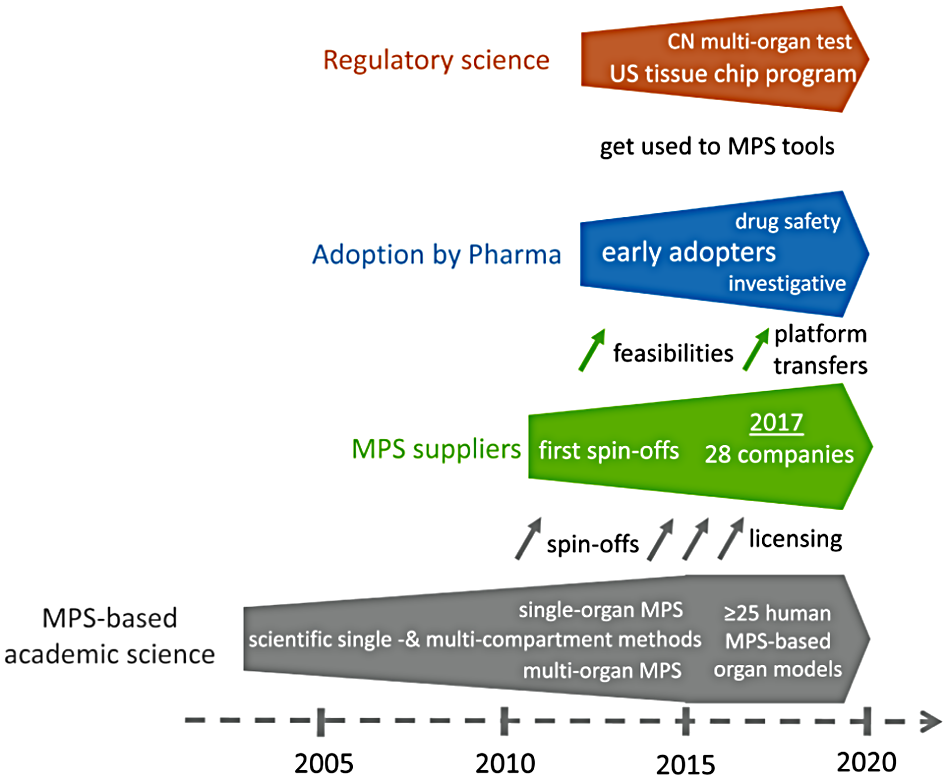

Figure 1.5.: Chronological scheme of OoC stakeholders and their connecting relations to one another [51]

Although the lack of validation is recognized as a limitation of OoCs, attention needs to be paid to how much value validation carries for OoCs. Generalized validation may be appropriate for highly standardized and widely applicable methods but might be considered unsuitable for emerging OoC devices. A universal validation approach can be unrealistic and very time-consuming to achieve. Instead, qualification of OoCs is a more preferred approach proposed by the Food and Drug Administration (FDA) and the European Medicines Agency (EMA) [52]. The qualification of OoCs would create a comparison between OoC-derived data and corresponding data generated by conventional preclinical drug development models illustrating whether OoC data shows the expected behaviour and can be used as a reliable predictor of human response (or in a better manner than the conventional methods) [52][51].

On the other hand, standardization will aid in the adoption of OoCs by pharmaceutical and industrial end users. However, it can hinder the progress of the young technology. Just like any early-stage technology, OoCs are currently undergoing continuous changes in useful OoC models resulting in variations in substrate materials, and cell sources/types. Standardization at this pivotal stage would hinder academic research through strict obligations and constraints [52]. Therefore, it is agreed by experts, including those present at the ORCHID committee, that standardization should be put off to a later stage to allow room for exploration, innovation and improvement. The main solution for the limitations highlighted here lies in adapting a collaborative mindset within all the MPS/OoC stakeholders (Figure 1.5) starting early in the process through academic research and climbing up the ladder towards the regulatory bodies involved. This collaborative mindset will create bridges between each stakeholder where exchange of information will occur resulting in the highlight of technical problems, and relevant solutions to tackle the problems through either already existing concepts or through the development of new concepts. Therefore, at this point, standardization and validation should be within the limitations of emerging OoCs to ensure that the technology can slowly transition to more generalized standardization and validation protocols without hindering innovation and improvement of the young technology. Specific technical problems can create a halt in the progress and create ambiguity in results obtained through OoCs due to the lack of a quantified system.

OoC Technical Readout Limitations

Readout technology is crucial for the proper evaluation of OoCs. Specifically, the readout of cellular metabolites is essential to evaluating how cultured cells are responding to the in-vitro microenvironment within the OoC. As a result, a variety of readout technologies were developed to assess the cellular conditions and responses inside the OoC, with the technology ranging from integrated sensors to sense the cellular microenvironment conditions (e.g. pH, temperature) [56], cellular activity (e.g. cell attachment, motility) [2], cellular metabolites [72] (e.g. metabolic byproducts, DNA), and bioelectricity [32]. In addition to integrated sensors, OoCs are great candidates for optical microscopy imaging methods due to the integration of optically transparent materials for in-situ monitoring. The imaging methods range from transillumination imaging (e.g. phase-contrast, holographic optofluidic imaging), fluorescence imaging (e.g. confocal fluorescence), and smartphone-based imaging (e.g. quantitative phase, lens-free imaging) with each method having one main objective – drawing information from cultured cells [9].

Needless to say, the main focus of almost all OoC readout technology is to evaluate cellular behaviour. Despite the existence of mechanical force readouts such as integrated strain gauges, traction force microscopy, and mechanical cantilevers, the focus is still strictly on the cells. This is mainly due to the traditional mechanical characterization techniques being limited by the scale, enclosed nature and constraining geometries of OoCs [55]. Consequently, the engineering elements of OoCs are under-evaluated and this bottleneck is carried on into the context of microfluidic OoCs. Specifically, the flow rate within microfluidic OoCs is considered a critical measurement of the system performance and changes to the flow can indicate problems occurring in the microfluidic system (e.g. bubble formation, leakage, blockage, surface fouling) [65]. In addition, microfluidic channels in OoCs are generally responsible for the transport of biological materials and chemical samples along with flow-induced stimulation to the cultured cells (e.g. fluid-induced shear stress). Therefore, the accurate control of these processes requires time-resolved flow dynamics within the micron-scale spatial resolution to faithfully dissect the flow behaviour, and aid in the optimization and design of microfluidic OoCs as well as validate the corresponding computational fluid dynamics (CFD) models. The small and complex

geometries of microfluidic OoCs can make analytical CFD models challenging and insufficient to predict the actual flow behaviour. In addition, varying microfabrication techniques, materials, and surface modifications/treatments such as material hydrophobicity, and surface roughness modifications can have unexpected effects on the flow properties creating a gap between idealized simulations and physical reality. The measurement of changes in flow rate can help identify system responses to such changes. On the other hand, having such measurements can help biologists create more novel and (patho)physiologically relevant results where the cultured cells are sensitive to flow-induced shear stresses [38].

1.3. Thesis Contribution

Currently, there are no widely accepted methods that can accurately measure real-time flow rates in microfluidic OoCs [65]. Due to the overlapping silicon wafer-based microfabrication processes that create OoCs and sensors, sensor-integrated OoCs are common [3][4][81][32] but almost all the sensors are to measure cellular metabolites or activity to quantify cell behaviour. On the other hand, the sensors designed for measuring flow rates (less than a handful) are only limited to localized measurements at the location of the sensor. As a solution, one might integrate an array of sensors to overcome the localized measurement limitation, but this makes the OoC design more complex and dependent on cleanroom-based microfabrication processes ultimately resulting in increased costs. On the other hand, optical imaging techniques such as particle image velocimetry [11] [10], particle streak velocimetry [43], and particle tracking velocimetry [27] exist but are usually dependent on dyed or fluorescent tracer particles which not only complicates the experimental procedures but also comes with additional factors associated with the photobleaching of the particles/dyes. To overcome the problems associated with fluorescent particles, one could implement particle tracking velocimetry to track individual high-contrast particles in sparsely seeded fluids but this comes with the trade-off in spatial resolution and specifically a poor spatial resolution near boundaries of the system, which makes the translation of measured flow rates to other biologically-relevant information, such as wall shear stress, challenging. Even though spatial resolution limitations can be alleviated with optimized confocal parameters of the optical system, such systems are still limited to only providing depth-averaged information making quantitative analysis of actual flow more difficult.

Therefore, this thesis research aimed to discover if optical coherence tomography (OCT), an optical imaging technique, is capable of quantitatively measuring flow rates inside a microfluidic OoC and possibly alleviate some of the aforementioned OoC limitations along with the limitations of other flow measurement techniques applied till today. Detailed descriptions of the microfluidic OoC system are in Chapter 2, followed by the OCT working principles in Chapter 3. The experimental methods are in Chapter 4 with the corresponding measurements in Chapter 5 which are discussed in Chapter 6 and concluded in Chapter 7.

2. Bi/ond Microfluidic OoC

2.1. inCHIPit™ –1C

Over the last decade, OoC research gained international recognition as a promising area of biomedical engineering with the first OoC developed in 2010 by Wyss Institute, Harvard [39]. The convergence of research efforts, funding, and regulatory incentives in Europe has created a robust knowledge ecosystem creating momentum in the biotechnology industry [21]. As a result, many companies, including a TU Delft spin-off company established in 2017 called Bi/ond, have sprouted with the effort of contributing to the acceleration of OoCs. The Bi/ond inCHIPit-1C™ is a 10x10 mm square (Figure 2.2, silicon-wafer based microfluidic OoC fabricated by cleanroom-based microfabrication processes (Figure 2.1). Detailed information on the microfabrication processes will not be discussed here and can be found in Chapter 8 of N. Gaio's PhD thesis [34].

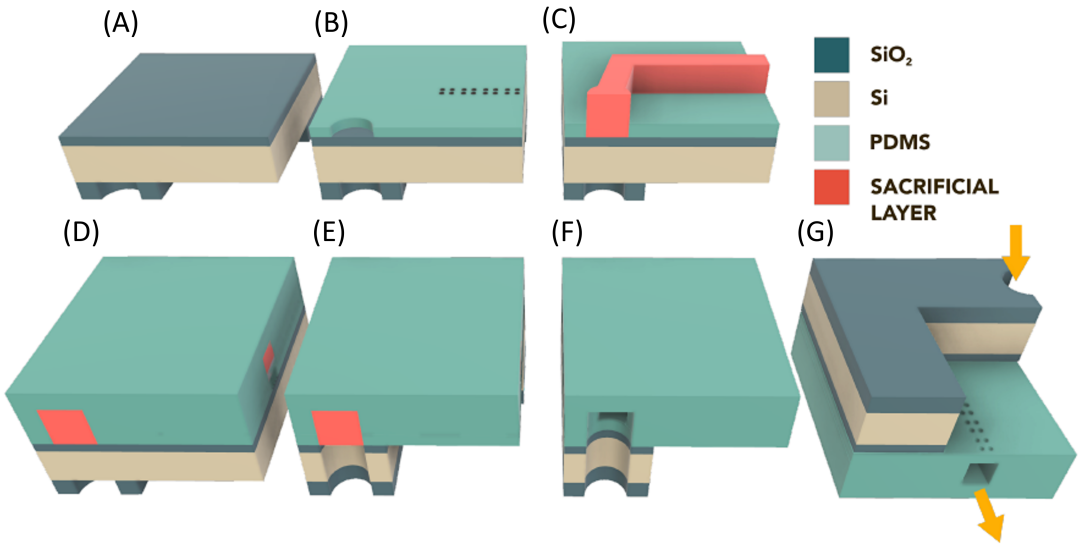

Figure 2.1.: Schematic illustration of the microfabrication steps to create the inCHIPit; (A) plasma enhanced chemical vapour deposition of SiO_2 on the back and front side of the wafer; (B) the PDMS is spin-coated on the wafer and patterned to create the porous membrane; (C) the sacrificial layer is deposited and patterned to create the microfluidic channel; (D) the second layer of PDMS is spin-coated to completely cover the sacrificial layer to later create the microfluidic channel; (E) the Si and SiO_2 are etched to create the inlet/outlet of the channel; (F, G) the sacrificial is removed [34]

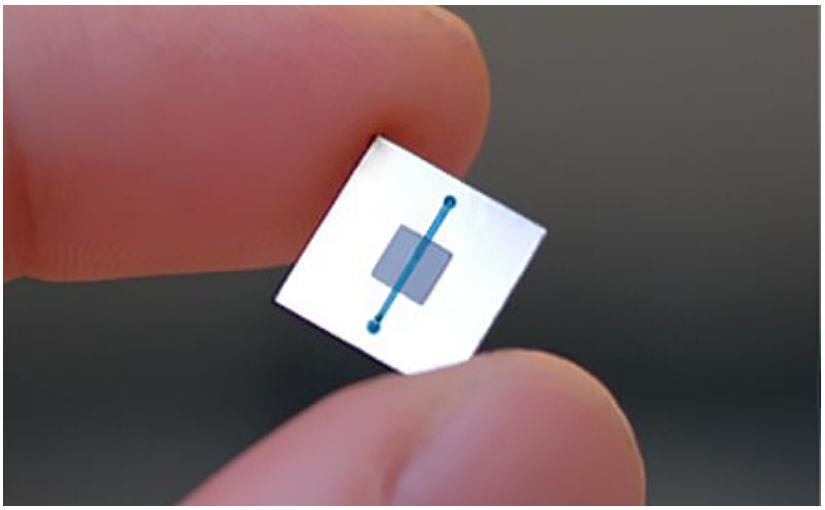

Figure 2.2.: The Bi/ond inCHIPit–1C held in-hand to visualize the dimensions of the OoC [34]

2.2. PDMS & Surface plasma treatment

The main feature of the inCHIPit–1C is a poly(dimethylsiloxane) (PDMS) microfluidic channel, with a porous membrane on the ceiling of the channel that leads to a static culture well. The flow going in and out of the system (via the inlet and outlet respectively) is the driving force of fluid movement inside the system and the porous membrane geometry creates an active perfusion flow inside the static culture well (Figure 2.3). The stiffness and porosity of the substrate stem cells reside on, ultimately regulate stem cell differentiation [77]. PDMS is the most common soft polymer used in OoCs, including the inCHIPit, due to its biocompatibility, gas permeability, optical transparency, chemical inertness, elasticity, and low-costs [45]. The fact that PDMS is a polymer means it can go through functional modification during the polymer synthesis processes that create it. This allows PDMS to have tunable mechanical properties (e.g. stiffness) along with topographies and surface functionalities, allowing researchers to tune it depending on the cell substrate needs which come in conjunction with the type of (stem) cells used in the in-vitro model [77]. As a result, PDMS becomes a highly versatile material allowing the incorporation of a dynamic, stimulating microenvironment into the inCHIPit system. The presence of microfluidic flow allows the cells residing on the substrate (with appropriate cell-adhesive coating) to be stimulated with flow-induced shear stress. The presence of pores provides a 3D microenvironment, allowing the cells to go through morphogenetic movement. Despite all the advantages, the hydrophobicity of PDMS is a drawback. The hydrophobic surface of PDMS makes cell seeding protocols challenging due to the very high contact angle of fluids on the surface, making cell-adhesive coatings difficult to apply. In the context of this research, the hydrophobicity of PDMS created technical challenges that make it a worthwhile topic to briefly reiterate despite the already well-documented mechanisms of PDMS hydrophobicity. The challenges are discussed in Chapter 6.

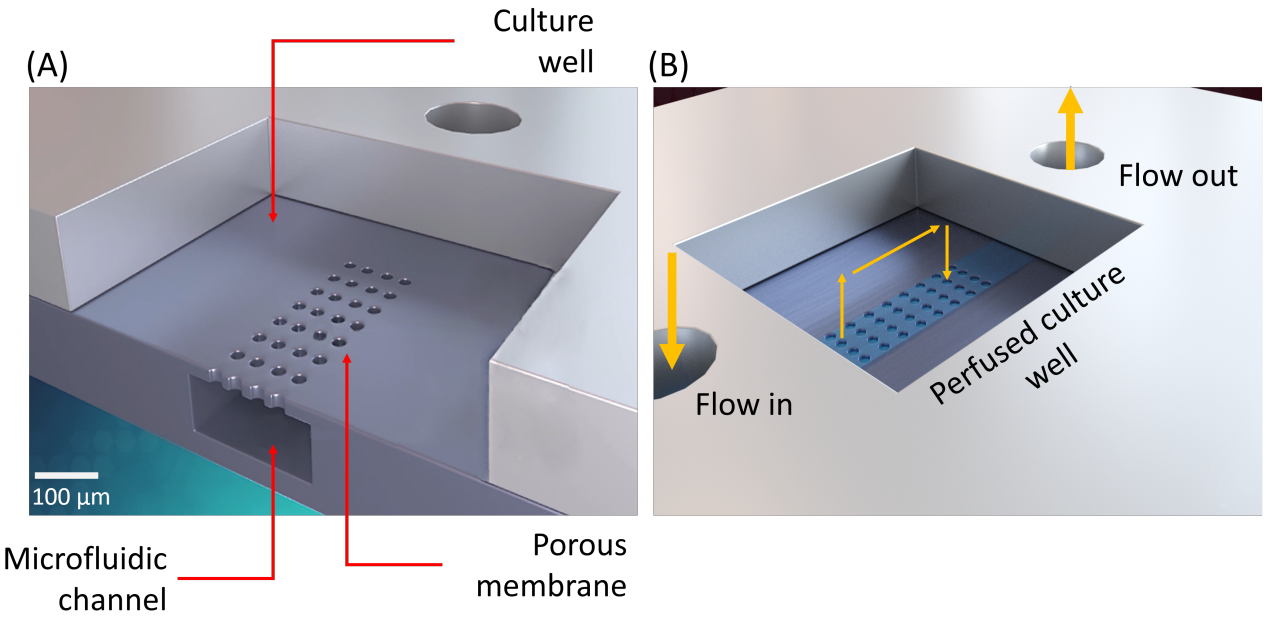

Figure 2.3.: Computer rendered images of the inCHIPit-1C (A) displaying the cross-section of the microfluidic channel, porous membrane and the static culture well and (B) the inCHIPit top view displaying the direction of flow from the inlet, through the microfluidic channel pores creating a perfusion area, and back out from the outlet [34]

The most commonly used method to increase the hydrophilicity of PDMS is via plasma surface modification [83]. The hydrophobic nature of PDMS occurs from the presence of the organic methyl groups present in the chemical structure of PDMS (Figure 2.4), resulting in a water contact angle (WCA) greater than 90° making it hard for the cells to adhere on the surface. The basic working principles of surface plasma treatment of PDMS are based on exposing the PDMS to ionized gas (commonly oxygen) in a vacuum chamber. In the case that the gas is oxygen, the methyl groups on the exposed surface of the PDMS are replaced with hydroxyl groups to create polar silanol groups, making the surface hydrophilic. This can decrease the WCA of PDMS by 30° or more depending on the treatment time [1] and not only significantly improve cell adhesion onto the surface but also increase the ease of fluid, and its constituents, passing through the porous PDMS membrane. The increased PDMS hydrophilicity in combination with appropriate cell-adhesive coating and the aforementioned standalone benefits of PDMS create a microenvironment that allows the culturing of cells (Figure 2.7).

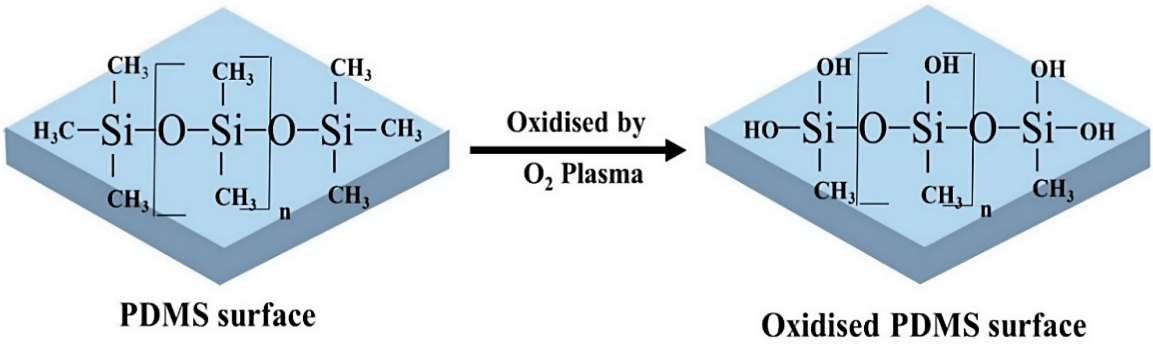

Figure 2.4.: Schematic illustrating the temporary surface functionalization of the PDMS to improve hydrophilicity of the surface [1]

2.3. inCHIPit™ microfluidic assembly

The inCHIPit was designed to be held by a housing – the comPLATE™. A customized version of the comPLATE (Figure 2.5) was used for this research that allowed easy placement of the assembly on the OCT stage (Figure 4.2). The side-view of the entire system along with the dimensions is visualized in Figure 2.6. The assembly allows the easy connection of the microfluidic pump to the OoC to achieve flow that can be recorded by the OCT optical beam through the observation window.

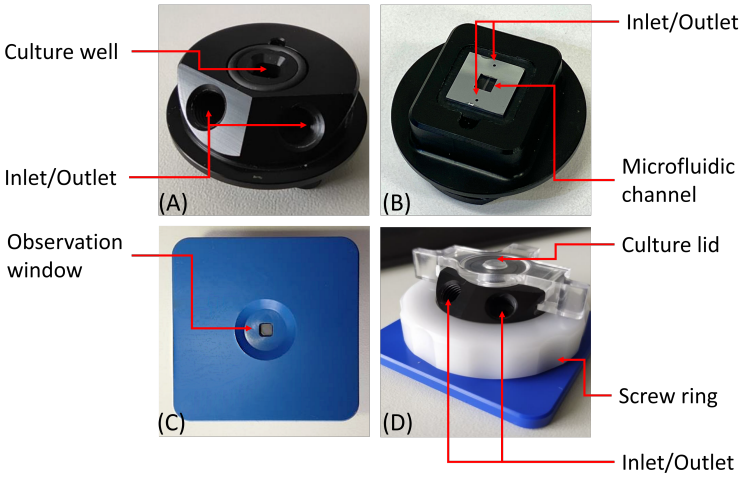

Figure 2.5.: Different housing components of the inCHIPit. (A) The top plate allows access to the culture well and the connection of tubing leading to the OoC placed on the (B) underside of the top plate. (C) The bottom plate holds the OoC in place and has an observation window that allows the system to be imaged optically. (D) The full assembly with the culture lid partially isolates the culture well from the environment. Modified from [66]

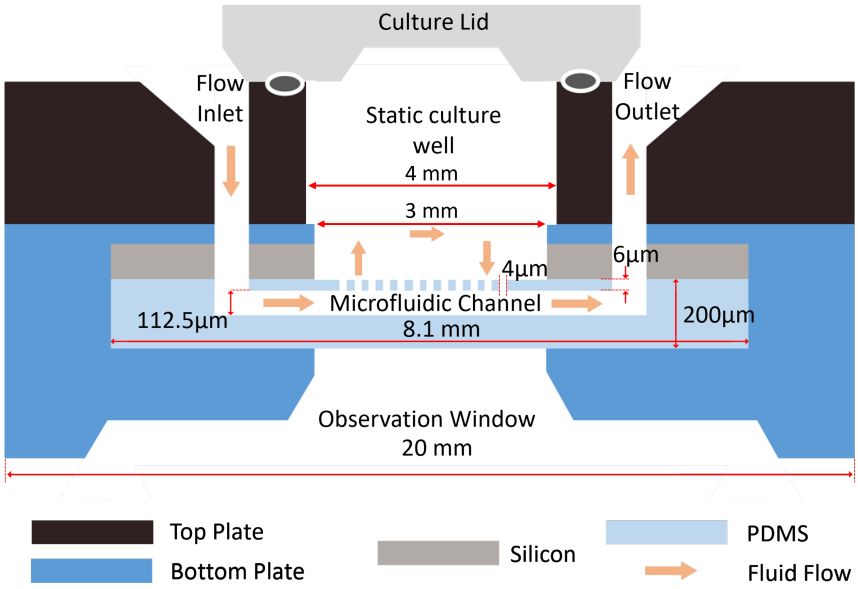

Figure 2.6.: Schematic of the inCHIPit assembled inside the custom bottom plate, displaying the internal dimensions of the system features along with the direction of fluid flow in and out of the system

2.4. inCHIPit™ with cells

The presence of PDMS and a porous membrane in the inCHIPit, along with flow-induced mechanical stimuli, creates a microenvironment that can facilitate cell (Figure 2.7A) and organoid (Figure 2.7B) growth. During this research, the effects of cell morphology on the flow inside the OoC were tested with varying cell culture conditions. Specifically, human umbilical vein endothelial cells (HUVECs) were cultured in the microfluidic channel and arising retinal pigment epithelia (ARPE19) were cultured in the static culture well, and finally a co-culture of both cell types as seen in Figure 2.7A. All cell cultures were fixed with paraformaldehyde after reaching a matured adhesion to the PDMS, resulting in the culture models being a morphological representation of the cells rather than a live cell culture.

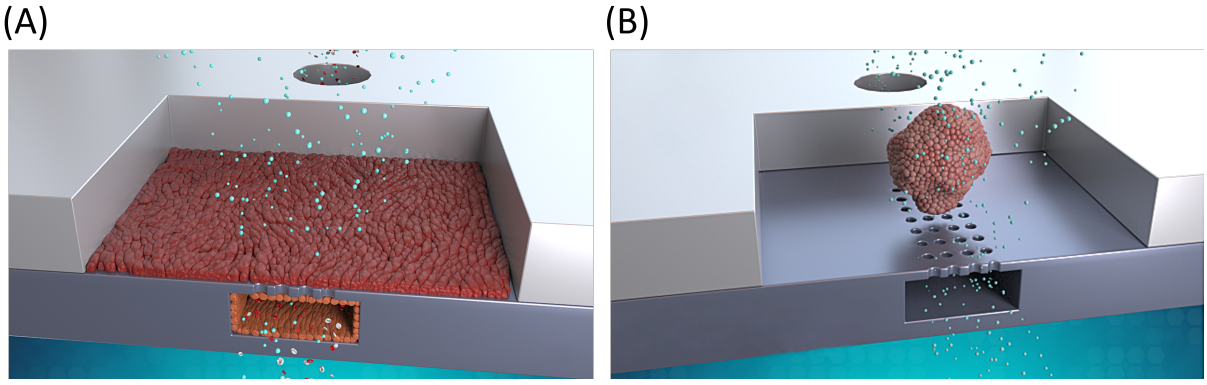

Figure 2.7.: Computer rendered images of the inCHIPit displaying the capabilities of creating (A) co-culture in-vitro models with endothelial cells inside the channel and epithelial cells in the culture well as well as (B) an organoid under perfusion inside the culture well [34]

3. Optical Coherence Tomography

OCT is an advanced, non-invasive, non-destructive optical imaging technique that can generate cross-sectional (1D or 2D) and volumetric (3D) images of the internal microstructure of samples in real-time at near-micron resolutions and with penetration depths reaching up to 3 mm [25]. OCT is considered an extension of a technique called low-coherence interferometry, initially applied to obtain in-vivo measurements of the eye axial length [30]. In-vivo cross-sectional images were also used to evaluate retinal diseases which eventually paved the path towards optical biopsy applications – the in-situ visualization of tissue microstructure without removing and processing tissues from the body [6] [25]. Nowadays, OCT is not only used in a variety of medical application areas such as dermatology [76] and angiography [23] but also in non-medical applications such as additive manufacturing [24], along with metrology and industrial-level material inspection [67].

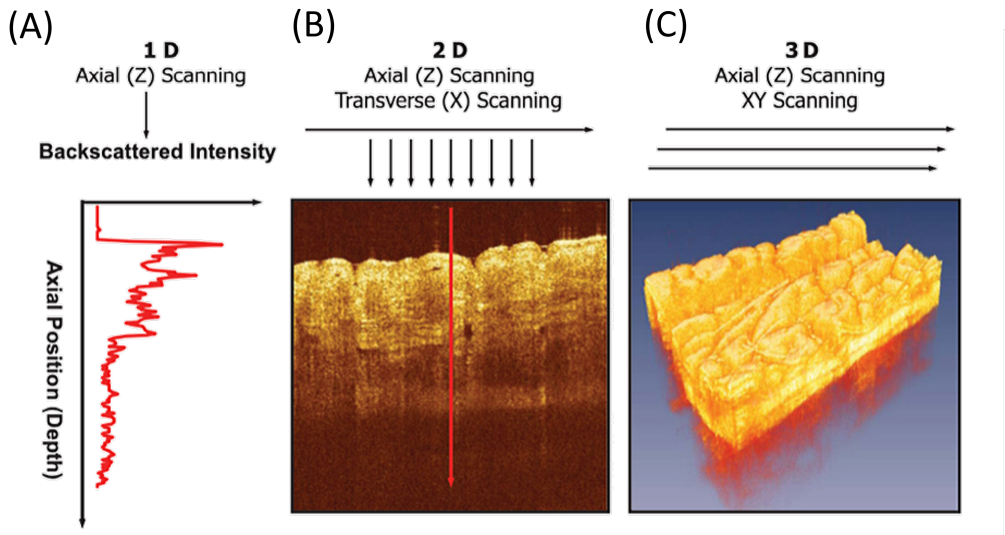

Figure 3.1.: Visualization of OCT generated cross-sectional and 3D images by the measurement of backscattered light. (A) Axial scans (A-scans or M-scans) measure backscattering versus depth. (B) Cross-sectional images are generated by a series of M-scans at varying transverse positions to create a 2D data set called B-scans. (C) 3D data sets are created by raster scanning B-scans, called C-scans. Modified from [25]

The general working principle of generating cross-sectional images with OCT is based on measuring the time-of-flight of light that backscatters from the sample using a Michelson interferometer [42]. The backscattered light creates an interference pattern between the light travelling through the sample arm and the light travelling through the reference arm of the Michelson interferometer. The information can be transformed to the refractivity-contrasted, internal structure of the sample along the penetration depth of the incident beam (z-direction) in a layer-by-layer manner represented by an intensity profile in the form of a reflectivity profile in depth.

This creates the basis for structural OCT. Scanning the sample axially (z-direction) in a single point generates 1D intensity profiles of the sample at that point, called A-scans or M-scans (Figure 3.1A). Scanning the sample axially while transversely (in the x or y-direction) moving the optical beam over multiple points generates 2D data-sets called B-scans (Figure 3.1B) and repeating the B-scans by raster scanning at varying transverse locations generates volumetric 3D data-sets called C-scans (Figure 3.1C). As a result, the location and relative strength of optically scattering structures can be determined and displayed with a depth-resolved intensity image that displays the layers of the structures that make up the sample (limited by the penetration depth of the optical beam).

Over the years several different OCT configurations have been developed with each having advantages and drawbacks, dependent on the intended application. Initially, OCT depth scans were obtained by mechanically scanning the reference arm of the Michelson interferometer over time to obtain time-encoded intensity signals of the sample and was called time-domain OCT (TD-OCT). Over the years, the implementation of broadband light sources improved axial resolutions (from 10 to 2 µm in tissue) [33]. The introduction of Fourier-domain OCT (FD-OCT) improved data acquisition speeds significantly by detecting backscattered signals in the frequency domain, allowing depth information to be measured without the movement of the reference mirror. Two FD-OCT types exist: spectral-domain OCT (SD-OCT) where depth data is acquired with a broad bandwidth light source, detected by a high-speed line camera and resolved with a spectrometer in space. In the case that a wavelength sweep over the broadband spectrum of a rapidly tunable laser source is performed in time, the process is called swept-source OCT (SS-OCT) [42]. The system used in this research was an SD-OCT, therefore the working principles of this system will be highlighted.

3.1. OCT Theory

3.1.1. Low Coherence Interferometry

Due to the high speeds of light, achieving an axial resolution of only 10 µm would demand a time resolution (30 femtoseconds) from the recording electronics of the system [25]. Since this is not realistically feasible, interferometric techniques are used to measure the small time differences. Figure 3.2 shows the principle of FD-OCT. The light source emits electromagnetic waves into a Michelson interferometer with a spectral intensity distribution $S(k)$, where the optical incident beam is split into two beams via a 50/50 beam splitter: a sample beam and a reference beam. The beam splitter reflects the beam with a reflection coefficient α and a transmission coefficient $1-\alpha$. The reference beam field gets reflected by the beam splitter, travels a distance L in the reference arm and gets reflected from the fixed reference arm mirror. After propagating back over length L, the field reaches the beam splitter and is transmitted to the detector. The sample beam transmits through the beam splitter and travels to the zero-delay line (equal optical path length for both sample and reference beam) and further into the sample where it gets backscattered from different interfaces at depth d (d_1, d_2 etc.). After being backscattered from the sample, the beam travels back to the beam splitter and gets reflected to the detector. The detector has either spatially-distributed pixels (SD-OCT) that sense the beams along with the resulting interference pattern $I(k)$ [42]. Alternatively, the light source sweeps rapidly in time over k where $I(k)$ is measured in time (SS-OCT). Ultimately, the intensity $I(k)$, as

a function of wavenumber k, is measured resulting in real-time information about the location (in space) and scattering efficiency of the structures that make up the sample [25].

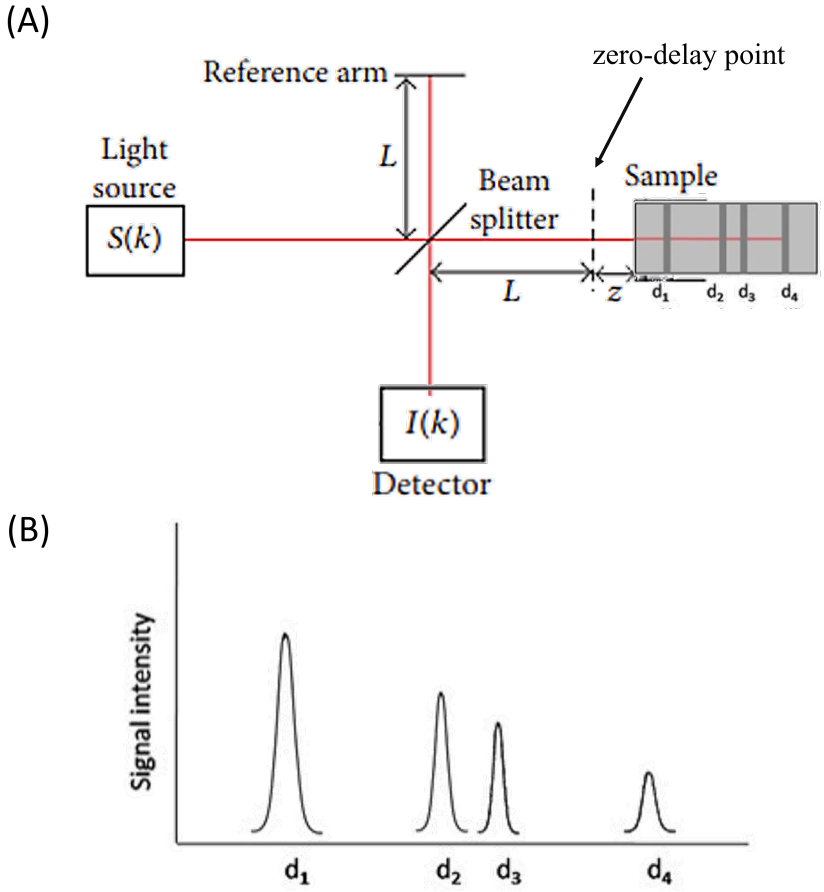

Figure 3.2.: (A) Schematic of a typical Michelson interferometer-based OCT system displaying how the time-of-flight and magnitude of the backscattered light determine the different interfaces within the sample (d_1, d_2 etc.) generating a corresponding intensity peak in (B) the reflectivity profile in depth. Modified from [50][42]

The source spectral intensity distribution $S(k)$ is a function of wavenumber $k = 2\pi/\lambda$. The intensity launched into the interferometer is described with [42]

$$I(k) = \left(\sqrt{S(k)}e^{j\phi(k)}\right)\left(\sqrt{S(k)}e^{j\phi(k)}\right)^{*} \tag{3.1}$$

where $\phi(k)$ is the randomly distributed phase of the radiators of the source (e.g. a superluminescent diode) and $*$ denotes the complex conjugation. Assuming a reference arm mirror with field reflectivity r_r, the reference arm field ($E_r(k)$), detected by the detector, is given by

$$E_r(k) = \sqrt{\alpha(1-\alpha)}r_r\sqrt{S(k)}e^{j\phi(k)}e^{j2kL} \tag{3.2}$$

The sample arm field, sensed by the detector, is given by the summation of all path lengths $\tilde{z} = 2z$ of the sample (since the beam travels to the sample and then back the same distance)

$$E_s(k) = e^{j\pi}\sqrt{\alpha(1-\alpha)}\sqrt{S(k)}e^{j\phi(k)}e^{j2kL}\cdot\int_{-\infty}^{\infty} a\left(\frac{\tilde{z}}{2}\right)e^{jkn(z)\tilde{z}}\,\mathrm{d}\tilde{z} \tag{3.3}$$

where $a(\tilde{z}/2) = a(z)$ is the complex-valued depth-dependent field reflection coefficient of the sample, and $n(z) = 1$ (the assumed refractive index distribution throughout the sample) [42]. The parameter z is the unidirectional path length difference and is defined as the depth (along the optical beam axis). In reality, the total intensity measured by the detector has three contributions – the reference arm intensity (usually subtracted from the signal), the sample arm intensity (very small for turbid samples), and the interference intensity [42]. Here, only the interference term ($I_{\text{int}}(k)$) is investigated and given by

$$I_{\text{int}}(k) = E_r(k)E_s(k)^* + E_s(k)E_r(k)^* \tag{3.4}$$

After some mathematical manipulation, the equation becomes

$$I_{\text{int}}(k) = \alpha(1-\alpha)S(k)r_r\int_{-\infty}^{\infty}\tilde{a}\left(\frac{\tilde{z}}{2}\right)e^{-jk\tilde{z}}\,\mathrm{d}\tilde{z} \tag{3.5}$$

where $\tilde{a}(\tilde{z}) = e^{-j\pi}a^*(\tilde{z}/2) + e^{j\pi}a(-\tilde{z}/2)$ is the symmetric representation of the sample reflectivity. Looking at Equation 3.5, the Fourier pair $\tilde{z} \leftrightarrow k$ can be seen as the multiplication of the source spectrum ($S(k)$) with the Fourier transform of $\tilde{a}(\tilde{z}/2)$. Therefore, the complex-valued depth-dependent OCT signal $i(\tilde{z})$ is

$$i(\tilde{z}) = \mathcal{F}_k^{-1}\{I_{\text{int}}(k)\}(\tilde{z}) = \alpha(1-\alpha)r_r\mathcal{F}_k^{-1}\{S(k)\}(\tilde{z}) * \tilde{a}\left(\frac{\tilde{z}}{2}\right) \tag{3.6}$$

where $*$ denotes the convolution operation. After substituting $\tilde{z} = 2z$ the OCT signal can be represented in terms of its amplitude

$$|i(z)| = \sqrt{\mathrm{Re}^2\{i(z)\} + \mathrm{Im}^2\{i(z)\}} \tag{3.7}$$

or intensity $|i(z)|^2$ of the complex-valued signal and can be plotted on a logarithmic scale to generate structural OCT images such as those in Figure 5.1. In addition, the axial point spread function (PSF) is given by the response of the signal $|i(z)|$ to a δ-function sample. In the case that the source generates a Gaussian-shaped spectrum with standard deviation σ_k and centre wavenumber k_c, the OCT axial PSF is

$$|i(z)| = \left|\frac{e^{-jk_c2z}}{4\pi}e^{-(2z)^2\sigma_k^2/2}\right| \tag{3.8}$$

Using Equation 3.5, the full width at half maximum (FWHM) of the Gaussian PSF in depth can be determined with $\mathrm{FWHM}_z = \sigma_k^{-1}\sqrt{2\ln 2}$. From $\mathrm{FWHM}_k = 2\sigma_k\sqrt{2\ln 2}$ and the relation between wavelength λ and wavenumber k, the FWHM_z is

$$\mathrm{FWHM}_z = \frac{2\ln 2}{\pi}\frac{\lambda^2}{\mathrm{FWHM}_\lambda} \tag{3.9}$$

FWHM_z is generally known as the round trip coherence length or in other words the axial resolution of the system (defined by the source spectrum characteristics) [42]. The transverse resolution is dependent on the focusing optics of the set-up and is determined by $\lambda/2\mathrm{NA}$ where NA is the numerical aperture of the objective the optical beam passes through.

3.2. Doppler OCT

The aforementioned OCT working principles not only capture structural information about the sample but simultaneously capture information about the translational motion of optically scattering particles. Specifically, the flow system in question can be seeded with optically scattering/contrasting particles that faithfully follow the flow in the system without themselves inducing an effect on the flow. The translational motion of the particles can be captured and the information can be embedded within the complex OCT signal (Equation 3.6) and retrieved with varying post-processing techniques. Doppler-OCT is one of the functional extensions of OCT that is used to measure the axial velocity vector component of the scattering particles in motion [44]. The early 2D in-vivo velocity imaging of blood flow was conducted in 1997 using Doppler-OCT [16][40]. The early Doppler-OCT systems worked based on obtaining frequency shifts by a spectrogram that used short-time fast Fourier transformation or wavelet transformation [40]. Such systems suffered from low sensitivity and limited imaging speeds that resulted in limited applications [48]. Due to the advent of SD-OCT in the early 2000s, phase-resolved Doppler-OCT was introduced and applied to imaging in-vivo vasculature [58]. The improvements in imaging speed and sensitivity of FD-OCT have also translated to improvements in phase-resolved Doppler-OCT. As a result, in-vivo imaging of blood flow velocity became possible with high spatial resolutions (2-10 µm) and high-velocity sensitivities (10 µm/s) [17]. In addition to medical applications, Doppler-OCT has been applied in measuring flows in microfluidic OoCs [46] and microfluidic channels [80].

The general working principle of phase-resolved Doppler-OCT is based on calculating the Doppler shift between adjacent A-scans, caused by particles moving through the optical beam that propagates through a flow channel (Figure 3.3). The flow channel is placed at an angle α with respect to the x-y plane. Due to refraction, the angle α can be different from the Doppler angle θ, which should be calculated based on Snell's law [8] to compensate for the refraction. Assuming that the flow is laminar, the transverse, $v_t(z)$, and axial, $v_z(z)$ velocity components can be expressed as a function of depth [13]. Given the geometrical configuration of the flow channel in Figure 3.3, and the total flow ($v_0(z)$), the velocity components can be defined as $v_t(z) = v_0(z)\cos(\theta)$ and $v_z(z) = v_0(z)\sin(\theta)$.

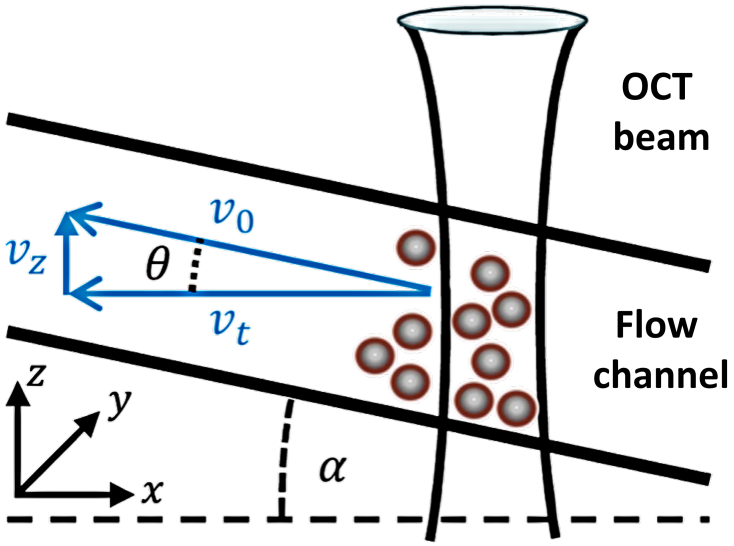

Figure 3.3.: Schematic of the optical beam propagating through the flow channel that is seeded with scattering particles following the fluid velocity (v_0). Modified from [13]

The movement of the particles through the optical beam causes a frequency shift of light that is backscattered from a particle undergoing axial motion [58]. As a result, the Doppler shift in the backscattered light causes a phase change, $\Delta\phi_{1,2}(z)$, between subsequent A-scans of the complex OCT signal $i(z)$ and is given by

$$\Delta\phi_{1,2}(z) = \angle e^{i(\phi_1 - \phi_2)} \tag{3.10}$$

Given the phase change for every acquired A-scan, the axial depth-resolved velocity $v_z(z)$ can be calculated using [13]

$$v_z(z) = \frac{\Delta\phi(z)}{q\Delta t} \tag{3.11}$$

where Δt is the sampling time and $q = 2nk_0$ is the scattering wavenumber with the refractive index of the medium being n and the vacuum wavenumber being k_0. The total velocity and its axial component are related with $v_0(z) = v_z(z)/\sin(\theta)$. Only at low transverse velocities, the maximum estimated axial velocity is limited by the Nyquist sampling criterion as

$$v_{z_{\max}} = \frac{\pi}{q\Delta t} \tag{3.12}$$

For high flow speeds the phase change, due to particles passing through the illuminating beam, does not increase linearly with increasing velocity [13]. Therefore, the phase change reaches a constant value, making the velocity unresolvable from phase changes. On the other hand, the minimum axial velocity of a given signal-to-noise ratio can be estimated with

$$v_{z_{\min,\mathrm{SNR}}} = \frac{2^{3/2}}{\pi q\Delta t\sqrt{\mathrm{SNR}\cdot M}} \tag{3.13}$$

where M is the statistically independent phase change measurements for calculating axial velocity. In other words, M is how many times the measurement is repeated, which increases the flow sensitivity by a factor of $\sqrt{M}$ [14].

3.3. Dynamic light scattering OCT

Dynamic light scattering (DLS) is a widely used technique that measures the flow or diffusion of particles in a given sample by analyzing the autocorrelation function of light backscattered from particles under motion. The earliest light scattering experiments were demonstrated by John Tyndall in 1868, where he characterized light backscattered from colloidal suspensions with particles larger than the incident light wavelength (Tyndall effect) [73]. Soon after, Lord Rayleigh evaluated light scattering from particles smaller than the wavelength of the incident light (Rayleigh scattering) which explained the reason why the sky is blue and described how the refractive index of the scattering medium plays a crucial role in light scattering [69][70]. Eventually, through the relationships developed by Einstein [28] and many other scientists [7][63] [31], the relations between light scattering and diffusion behaviour of particles were established and verified experimentally to characterize molecules in solution using light-scattering methods [68].

DLS-OCT, just like Doppler-OCT, is another functional OCT technique that can measure the diffusion coefficient and velocity vectors (axial and transverse) of particles in motion. Due to coherence gating used in OCT, the backscattered light can be collected only from a small sample volume, facilitating high-resolution 3D imaging of diffusion and flow [47]. Specifically, it is assumed that in a sample solution particles that are static and moving are mixed within the OCT resolution volume and the moving particles can either exhibit diffusive or translational motion [47]. Therefore, fitting algorithms are used to estimate dynamic parameters such as axial and transverse velocities of particles as well as the diffusion coefficient. The typical geometry, similar to Doppler-OCT, is shown in Figure 3.4. Just like the Doppler-OCT geometry, the flow channel is placed at an angle α with a difference from θ due to refraction, with θ being the angle the scattering particles follow within the channel due to channel geometry. $v_z(z)$ and $v_t(z)$ are the axial and transverse velocity components of the particles as a function of depth, respectively, and are defined as $v_t(z) = v_0(z)\cos(\theta)$ and $v_z(z) = v_0(z)\sin(\theta)$. The Gaussian OCT beam can be characterized by a beam waist w_0 in focus with a local beam waist $w(z)$ at a given location z along the optical axis (z-direction). The combination of the Gaussian-shaped lateral intensity and the axial coherence function results in the OCT PSF in the z and r-directions [14]

$$I(r,z) = \mathrm{e}^{-\frac{4r^2}{w^2(z)}}\mathrm{e}^{-\frac{2z^2}{w_z^2}} \tag{3.14}$$

where r is the radial distance from the beam centre, z is the axial position, and w_z is the coherence function waist in the sample, where the beam waist is defined as a distance from the beam centre where the beam intensity is e^{-2} of its maximum value. The coherence function waist is given by $w_z^{-1} = \sqrt{2}\sigma_k n$ where σ_k is the Gaussian source spectrum wavenumber standard deviation and n is the sample refractive index.

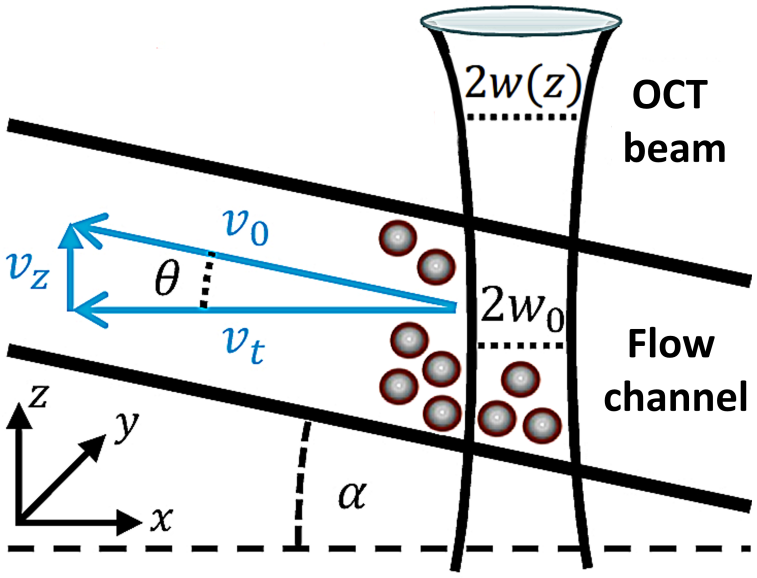

Figure 3.4.: Schematic of the optical beam, with a beam waist w_0 and local beam waist $w(z)$, propagating through the flow channel that is seeded with scattering particles following the total fluid velocity (v_0). Modified from [14]

3.4. Conventional DLS-OCT

In conventional DLS-OCT with non-dilute solutions, the measurement of flow is dependent on the light intensity fluctuations and is sensitive to both axial and transverse flows. For a Gaussian illuminating beam and Gaussian-shaped spectral envelope, the normalized depth-dependent autocovariance of the backscattered complex OCT signal is given by [13]

$$g_1(z,\tau) = A_1(z)\mathrm{e}^{iqv_z(z)\tau}\mathrm{e}^{-Dq^2\tau}\mathrm{e}^{-\frac{v_0^2(z)\sin^2\theta\,\tau^2}{2w_z^2}}\,\mathrm{e}^{-\frac{v_0^2(z)\cos^2\theta\,\tau^2}{w_0^2}} \tag{3.15}$$

where τ is the autocovariance time lag, $A_1(z)$ is the autocovariance amplitude containing the effect of a diminishing SNR, q is the scattering wavenumber (same as Doppler-OCT), and D is the particle diffusion coefficient. The decay rate of the OCT signal intensity can be expressed with the normalized second-order autocovariance [13]

$$g_2(z,\tau) = |g_1(z,\tau)|^2 = A_2(z)\mathrm{e}^{-2Dq^2\tau}\mathrm{e}^{-\frac{v_0^2(z)\sin^2\theta\,\tau^2}{w_z^2}}\,\mathrm{e}^{-\frac{2v_0^2(z)\cos^2\theta\,\tau^2}{w_0^2}} \tag{3.16}$$

Here, $A_2(z)$ is the depth-dependent amplitude factor. Equation 3.16 assumes that the average number of particles in the scattering volume, N, is sufficiently large ($N \gtrsim 100$), ensuring that the particle probability distribution in the scattering volume and corresponding backscattered light fluctuations follow Gaussian statistics. In OCT, N corresponds to the depth-resolved number of particles per scattering volume as a function of axial position z through the OCT beam shape. The expected number of particles in the scattering volume is a function of the PSF and the particle volume fraction f_v given by

$$\langle N \rangle = \frac{3 f_v V_s}{4\pi a^3} \tag{3.17}$$

where a is the particle radius and V_s is the scattering volume.

Since diffusion and flow decay functions multiply each other in $g_2(z,\tau)$, the flow decay must dominate over the diffusion decay to accurately determine the flow velocity. Hence, for flow decay to dominate, $\tau_{v_0} \ll \tau_D$ where τ_{v_0} and τ_D are the dynamic time constant of flow and diffusion decorrelations, respectively and are defined by [14]

$$\tau_D = (2Dq^2)^{-1} \tag{3.18}$$

and

$$\tau_{v_0} = \left(v_0 \sqrt{\frac{\sin^2\theta}{w_z^2} + \frac{2\cos^2\theta}{w^2(z)}} \right)^{-1} \tag{3.19}$$

resulting in the relation

$$v_0 \sqrt{\frac{\sin^2\theta}{w_z^2} + \frac{2\cos^2\theta}{w_0^2}} \gg 2Dq^2 \tag{3.20}$$

In the case that both decays are equally strong, the minimum measurable total velocity becomes limited by diffusion and is given by [14]

$$v_{0_{\text{min, }Diff}} = 2Dq^2 \left[\frac{\sin^2\theta}{w_z^2} + \frac{2\cos^2\theta}{w_0^2} \right]^{-1/2} \tag{3.21}$$

The minimum measurable velocity is also limited by the SNR, therefore the overall minimum total velocity limit is given by

$$v_{0_{\text{min}}} = \sqrt{v_{0_{\text{min, SNR}}}^2 + v_{0_{\text{min, Diff}}}^2} \tag{3.22}$$

3.5. Number fluctuation DLS-OCT

Number fluctuation DLS-OCT works based on obtaining flow measurements with the presence of a low number of particles in the scattering volume ($N \ll 100$). Using a low number of particles in the scattering volume generates additional correlations in the intensity due to fluctuations in the total number of scatters detected in the scattering volume [14]. Given the dilute, low particle limit the normalized second-order autocovariance function is given by

$$g_2(z,\tau) = \underbrace{|g_1(z,\tau)|^2}_{\text{Gaussian term}} + \underbrace{\langle \delta N(0) \delta N(\tau) \rangle}_{\text{number fluctuation term}} \tag{3.23}$$

where the first term is named the Gaussian term, while the second is the non-Gaussian, number fluctuation term. Incorporating the effects of SNR and a light beam with a Gaussian lateral and axial PSF, the total normalized second-order autocovariance function is given by

$$g_2(z,\tau) = \frac{1}{\left(1+\frac{1}{\mathrm{SNR}(z)}\right)^2}\frac{2^{3/2}\langle N\rangle}{2^{3/2}\langle N\rangle+1}\left[e^{-2Dq^2\tau}e^{-\frac{v_0^2(z)\sin^2\theta\tau^2}{w_z^2}}e^{-\frac{2v_0^2(z)\cos^2\theta\tau^2}{w_0^2}}\right. \\ \left. + \underbrace{\frac{1}{2^{3/2}\langle N\rangle}e^{-\frac{v_0^2(z)\sin^2\theta\tau^2}{w_z^2}}e^{-\frac{2v_0^2(z)\cos^2\theta\tau^2}{w^2(z)}}}_{\text{number fluctuation term}}\right] \tag{3.24}$$

For the scenario where N is sufficiently small and flow decorrelation is much smaller than diffusion decorrelation ($\tau_{v_0} \gg \tau_D$), contrary to the scenario in Equation 3.16, the normalized second-order autocovariance function is given by

$$g_2(z,\tau \gg \tau_D) \approx \frac{1}{\left(1+\frac{1}{\mathrm{SNR}(z)}\right)^2}\frac{1}{2^{3/2}\langle N\rangle+1}e^{-\frac{v_0^2(z)\sin^2\theta\tau^2}{w_z^2}}e^{-\frac{2v_0^2(z)\cos^2\theta\tau^2}{w^2(z)}} \tag{3.25}$$

where the Gaussian term has already decayed due to the larger time delays, and therefore g_2 is completely dominated by the number fluctuation terms. As a result, by using lower sample concentrations the flow and diffusion decorrelations are decoupled, and the minimum measurable total velocity is significantly lowered contrary to conventional DLS-OCT and Doppler-OCT [14].

4. Materials & Methods

4.1. OCT System

All the experiments for this research were conducted using the Thorlabs GANYMEDE II HR series spectral-domain OCT system operated with an NA = 0.05 scan lens (LSM04-BB, Thorlabs). The system bandwidth was centred around 900 nm with an axial resolution of 3 µm in air. Depending on the region of interest to be probed in the microfluidic OoC, the OCT was operated both in M-scan and B-scan modes with varying acquisition rates. During M-scan acquisition, subsequent A-scans were obtained at three different, fixed locations along the microfluidic channel. In B-scan acquisition, the optical beam was moved laterally, while simultaneously acquiring A-scans during the beam movement. The beam was moved laterally in the x-direction to obtain depth-resolved data along the length of the microfluidic channel. The beam was moved laterally in the y-direction to obtain depth-resolved data along the width of the microfluidic channel to create cross-sectional measurements. The scan orientations are illustrated in Figure 4.1.

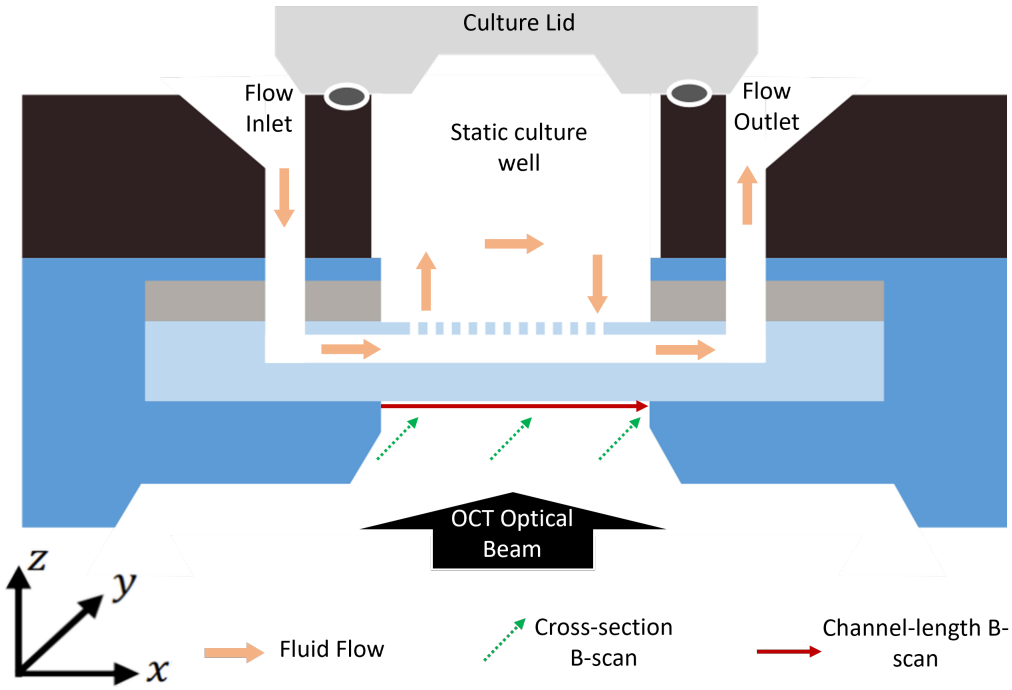

Figure 4.1.: Schematic displaying the acquired measurements at different locations in the OoC system. The optical beam swept laterally (y-direction) along the width of the channel creates cross-sectional images of the channel and culture well. The optical beam swept along the length of the channel laterally (x-direction) showing the length of the channel and the corresponding locations inside the culture well. M-scans were obtained at the same locations as the cross-sectional B-scans to generate 1D data along the z-direction only

4.2. Experimental Setup

The experimental setup displayed in Figure 4.2 was used for all the experiments conducted for this research with slight variations depending on the region of interest probed in the OoC and the OCT technique used. The microfluidic pump (built in-house by Bi/ond) pushed the particle-seeded fluid through the microfluidic tubing followed by the OoC assembly, and back to the reservoir. The multiaxial sample stage was used to have control over angle α and to reflect the specular optical beam reflections to the environment instead of the detector. The OCT reference arm, along with the probe height, was used to bring the region of interest in the OoC into focus to ensure a strong signal and high lateral resolution.

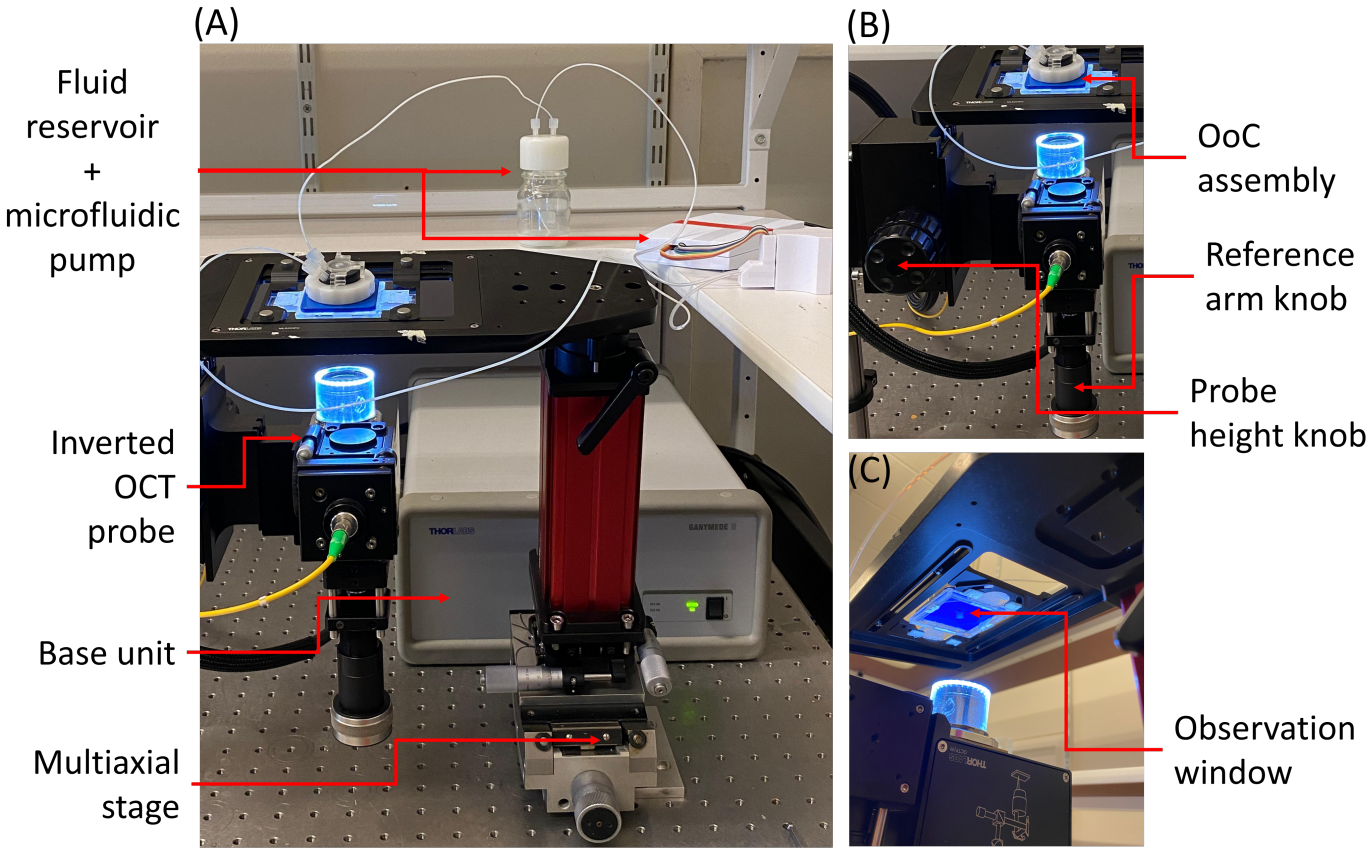

Figure 4.2.: Images of the OCT setup displaying (B) the placement of the OoC assembly on the multiaxial stage while connected to the microfluidic pump and (C) the optical beam (not visible) lined up with the observation window found on the underside of the OoC assembly

4.3. General OCT Post-processing

The base unit of the OCT system contains the superluminescent diode (SLD) that functions as the low-coherent, broadband light source. The spectrometer has 2048 spatially-distributed pixels. After the acquisition, the measured spectrum is resampled to a linearly-sampled wavenumber domain (k-domain) to ensure equidistant samples in the frequency domain. Next, the spectrum is apodized using a Gaussian window to form a Gaussian profile to reduce side slopes in the cross-correlation function. Ultimately, the spectrum goes through an inverse fast Fourier transform to obtain the depth-resolved complex OCT data. This was the general post-processing

workflow that was performed for every OCT measurement, regardless of the technique used. The general OCT post-processing script was written by Jos de Wit and was modified accordingly depending on the OCT technique used in this research.

4.4. Doppler-OCT measurements

During data acquisition for Doppler measurements, the multiaxial stage was adjusted in a manner that ensured the microfluidic channel was creating the lowest possible channel angle α (and consequently Doppler angle θ) with the absence of polluting reflections. Before introducing flow to the system, varying scans (M-scans & B-scans) were obtained to inspect system integrity. Next, B-scans along the length of the channel were obtained to measure the stage angle ($\alpha = 10.5$ °) through the Thorlabs software with slight variation for each experiment due to OoC alignment and microfabrication differences. The relatively high flow velocities (2-20 mm/s) in the microfluidic channel (compared to the culture well) deemed Doppler measurements most suitable for measurements inside the channel due to the high maximum measurable velocities using phase-resolved Doppler OCT. All Doppler measurements were conducted with 0.06% volume fraction intralipid (Sigma-Aldrich) suspended in water as scattering particles. Due to low concentrations, the solution refractive index was assumed to be the same as water ($n = 1.33$).

To obtain 1D Doppler flow measurements along the height of the channel, M-scans were taken at three locations - near the inlet, at the centre, and near the outlet of the microfluidic channel (Figure 4.1). The M-scans were made up of 31000 adjacent A-scans, where each measurement was repeated 5 times (M=5). The acquisition rate was varied depending on the expected flow velocities (5.5 kHz for a pump discharge of 5 µl/min and 36 kHz for anything above). The phase change between each adjacent A-scan was calculated to obtain the axial velocity. The axial velocity was then converted to total velocity by dividing the axial velocity with $\sin\theta$. To obtain 2D measurements along the width of the channel, cross-sectional B-scans were obtained in the same locations as the M-scans. The B-scans were made up of 20000 A-scans and repeated 20 times acquired at varying scanning rates similar to the M-scans. The same B-scan measurements were repeated for OoCs with the presence of fixed cells and the aforementioned process was repeated to calculate absolute velocity. Konstantine Cheishvili wrote the post-processing script [15] and a modified version of this script was used to generate the results.

4.5. Number fluctuation DLS-OCT measurements

The initial steps for inspecting the system before starting flow measurements were the same as described in the previous section. The relatively low flow velocities (0-120 µm/s) in the culture well of the OoC deemed number fluctuation measurements the most suitable for this region of the OoC. All number fluctuation measurements were performed with 0.005 % volume fraction of dilute monodisperse polystyrene scattering particle suspensions in water. The particles were supplied by InProcess-LSP with a particle radius of 257 nm and an assumed refractive index of $n = 1.33$ due to very low concentration. The acquisition rate for all measurements was set to 5.5 kHz.

After inspection, flow with the seeded particles was introduced into the system using the microfluidic pump. Two sets of measurements were taken - a calibration measurement and 2D

flow measurements. The calibration measurement was composed of a B-scan made up of 8192 A-scans and was performed inside the culture well filled with particles, with no active flow (static conditions). This measurement was repeated 20 times. Next, the pump was activated and B-scans at varying scanning planes (shown in Figure 4.1) and varying pump discharge rates were obtained. The B-scans were composed of 200 A-scans and the measurements were repeated 2000 times.

To quantitatively measure the flow, a calibration step was performed to experimentally determine the local beam waist $w(z)$ of the OCT beam by scanning the beam with a known velocity over the stationary sample. The local beam waist $w(z)$ was obtained by performing a fit of Equation 4.1 to the measured autocovariance functions

$$g_2(z, \tau > \tau_N) = A(z) \mathrm{e}^{-\frac{v_0^2(z) \sin^2 \theta \tau^2}{w_z^2}} \mathrm{e}^{-\frac{2v_0^2(z) \cos^2 \theta \tau^2}{w^2(z)}} \tag{4.1}$$

where τ_N is the time delay that ensures the diffusive term in the measured autocovariance had decayed sufficiently, and θ was assumed to be zero due to the physical orientation of the OoC system and the presence of no flow. In the fit, $A(z)$ and $w(z)$ are the free parameters. Once the calibration fit was complete the beam shapes were fitted using $w(z) = w_0 \sqrt{1 + (((z - z_0)/n)/z_R)^2}$ to determine the in-focus beam waist in the sample to be $w_0 = 6.61 \mu m$. The measured $w(z)$ was averaged and therefore assumed that the beam shape was constant rather than varying in depth. Next, a second fit of Equation 4.1 was performed, this time to determine the flow. Usually, there is a second calibration step to determine θ using flow measurements that have a sufficient Doppler signal but due to the low velocities in the culture well of the system (lower than measurable velocities with B-can Doppler acquisition), θ was not determined. Therefore, Equation 4.1 was mathematically manipulated to remove the dependency on θ and create the relationship

$$g_2(z, \tau > \tau_N) = A(z) \mathrm{e}^{-\frac{v_0^2(z) \tau^2}{w_z^2}} \mathrm{e}^{-\frac{2v_0^2(z) \tau^2}{w^2(z)}} \tag{4.2}$$

The OCT interference data was apodized with an apodization value of 118 pixels. This ensured that the averaged local beam waist $w(z)$ was numerically equated to the coherence function waist w_z in Equation 4.2, allowing the absolute velocity v_0 to be determined by fitting the equation to the measured autocovariance functions. This manipulation introduced roughly 15-25% error on the measured velocity at the edge of the axial range.

5. OCT measurements of microfluidic OoC

The OCT methods described in the previous chapter were applied to obtain quantitative measurements of flow velocity inside the OoC at different regions of the system and compare them to the corresponding theoretical predictions of flow as well as CFD simulations. Further in the research, biological applications relevant to the OoC were applied to draw quantitative data on flow velocity for the biological system. The experiments aimed to get an assessment of the use of OCT for application to microfluidic OoCs. The results presented in this chapter are generated by measurements taken at different locations in the OoC system, see Figure 4.1. Depth-resolved intensity images were generated at the corresponding locations. Figure 5.1A shows the cross-section of the OoC microfluidic channel and Figure 5.1B shows a different scanning plane that shows the channel length.

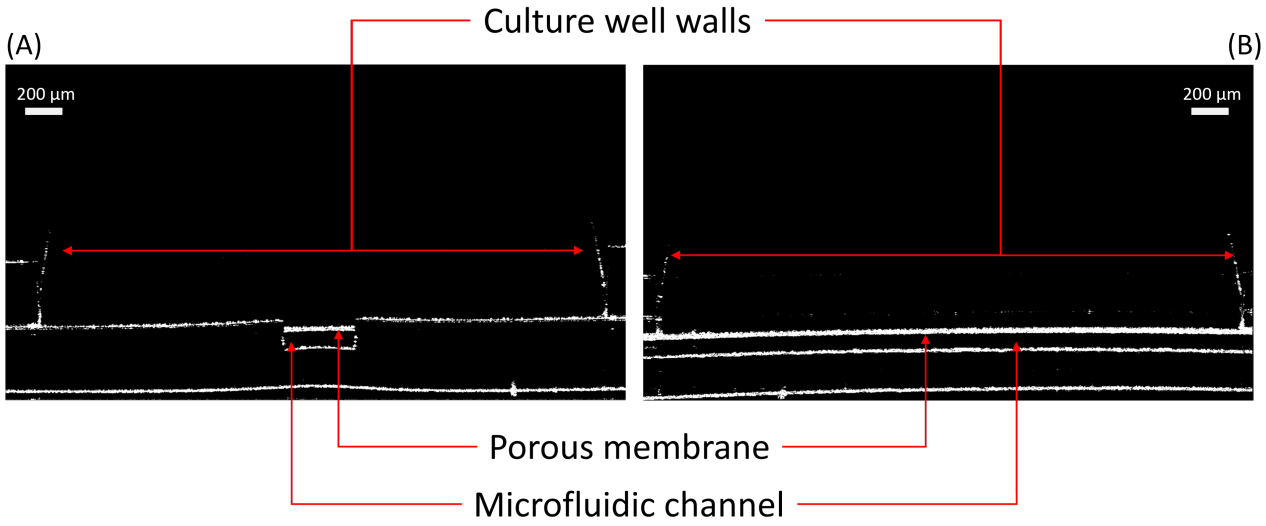

Figure 5.1.: OCT B-scan measurements of the OoC generating a depth-resolved structural intensity image in decibels (dB) contrasted by the differing refractivity of the materials that make up the OoC. (A) Cross-sectional B-scan generates an image that represents a slice of the microfluidic channel (channel going into and out of the screen). (B) A B-scan along the length of the channel generates an image that displays the channel length as far as the entire length of the culture well (3 mm)

5.1. OoC with no pores

Flow measurements were performed in the OoC without a porous membrane. The parabolic flow profiles in Figure 5.2A were generated with 1D M-scans taken at the centre point of the OoC microfluidic channel length. The flow profiles were generated by measuring the velocity of the flow at varying depths along the height of the channel. The width of the parabolic curve

represents the height of the channel (100 µm). The profiles show that the velocity of flow is zero at the boundaries of the channel (located at depths 80 and 180 µm) and the highest velocity is at the middle point of the channel height (130 µm). This occurrence holds for pump discharge rates of 5 and 10 µl/min but the remaining higher discharge rates produce slightly different outcomes. The boundary zero velocity locations differ with the first zero velocity location being 78 µm instead of 80 µm and the next at around 183 µm instead of 190 µm. In other words, the height of the channel for these high discharge rate measurements was increased to 105 µm. The effects of this geometric shift are visualized in Figure 5.2B where the experimental maximum velocities (apex of parabolic flow) were compared to the theoretical expectations of the maximum velocity at the corresponding pump discharge rates. The experimental trend shows an increasing deviation from the theoretical results as the pump discharge rate increases and this is also depicted from the slope of the linear fits for both the experimental and theoretical maximum velocities. In other words, the higher the discharge rate, the higher the deviation from the theoretical expected maximum velocity in the centre of the channel.

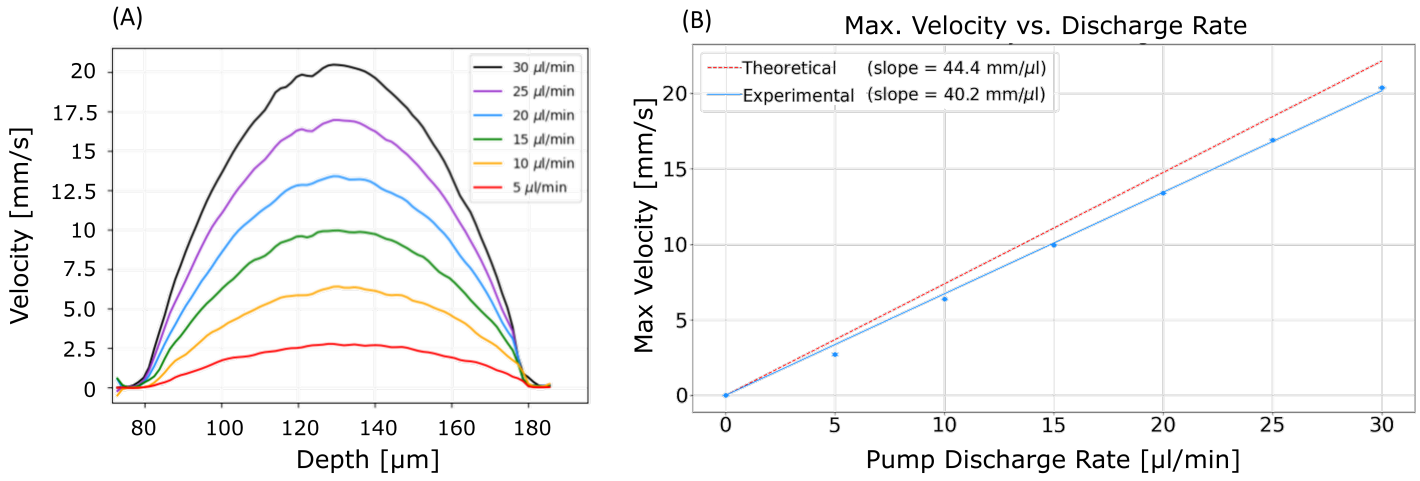

Figure 5.2.: 1D M-scans of the inCHIPit without a porous membrane acting as a simple rectangular PDMS microfluidic channel. (A) Parabolic flow at the centre of the channel for differing pump discharge rates. (B) A linear fit of the maximum velocity (apex of parabolas) measured in the channel compared with the expected theoretical flow for a rectangular channel with the same dimensions and corresponding pump discharge rates

The 2D flow velocity profiles in Figure 5.3A were generated with cross-sectional B-scans of the microfluidic channel and compared to the corresponding CFD simulations (Figure 5.3B) for the same pump discharge rate. The measurement shows the flow velocity distribution along the width and height of the microfluidic channel. Just like the 1D measurements, the velocity at the boundaries of the channel is zero. The highest velocity was recorded at the centre of the channel at about 23 mm/s. The colour bar range of the experimental results was matched with the simulation for a trustworthy comparison of the velocity distribution. The qualitative comparison with the simulation result shows a good agreement with the velocity distribution but a slight disagreement in the velocity values. The cross-sectional measurement also shows the channel height to be around 90 µm and the width to be around 400 µm. Note that the simulation dimensions are 100 by 400 µm.

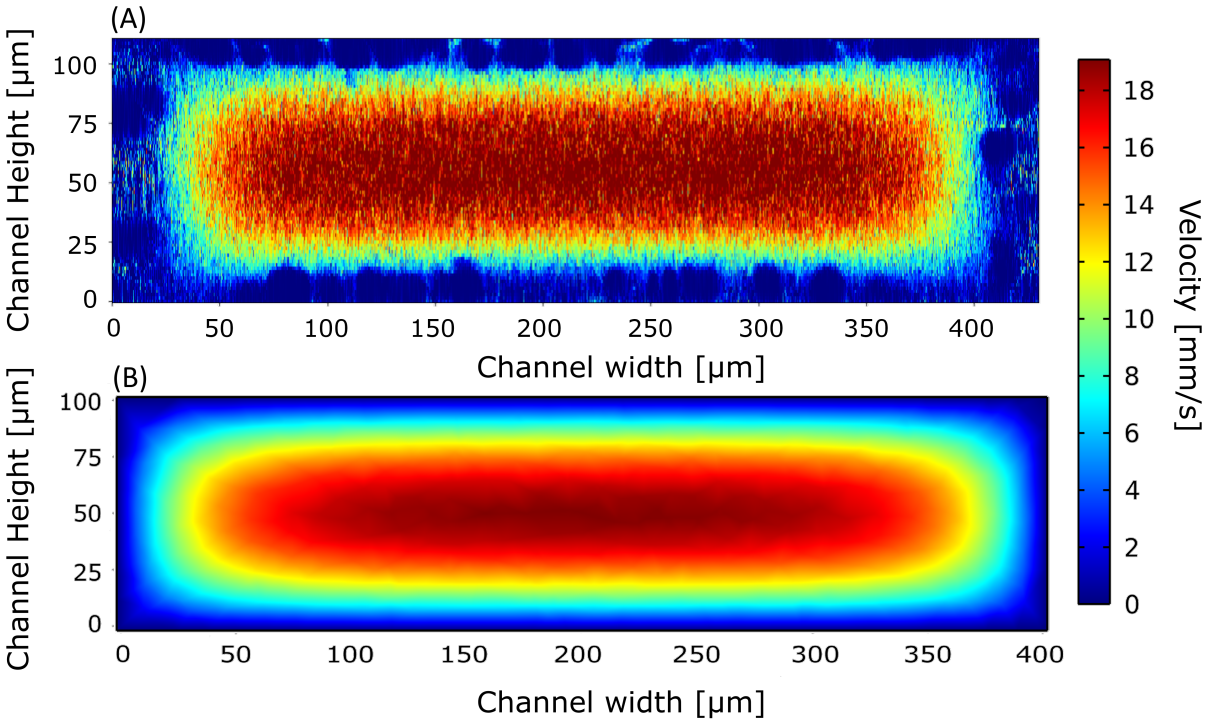

Figure 5.3.: (A) Cross-sectional B-scan of the inCHIPit with no pores displaying the 2D velocity distribution along the width and height of the microfluidic channel created by a pump discharge rate of 25 µl/min. (B) Corresponding COMSOL simulation of flow through a static rectangular channel at the same pump discharge rate [64]

5.2. OoC with pores

The measurements in this section were taken in the OoC with the presence of pores and the perfusion flow inside an empty culture well of the system was evaluated. Figure 5.4A displays the velocity distribution of the fluid inside the culture well where the inlet is located on the right of the figure and the outlet on the left. The experimental data show that the velocity distribution pattern within the culture well was a good match with the corresponding simulation results in Figure 5.4B. The overall trend was that the velocity of the fluid exponentially decreases as it gets farther away from the channel porous membrane (inlet) and speeds up again as it circles back to the porous membrane (outlet). It can also be observed that the lowest velocity is always at the very centre of the culture well. Small streaks near the centre of the well illustrate the turning point of the fluid direction from about 23 µm/s close to 0 µm/s at the very centre.

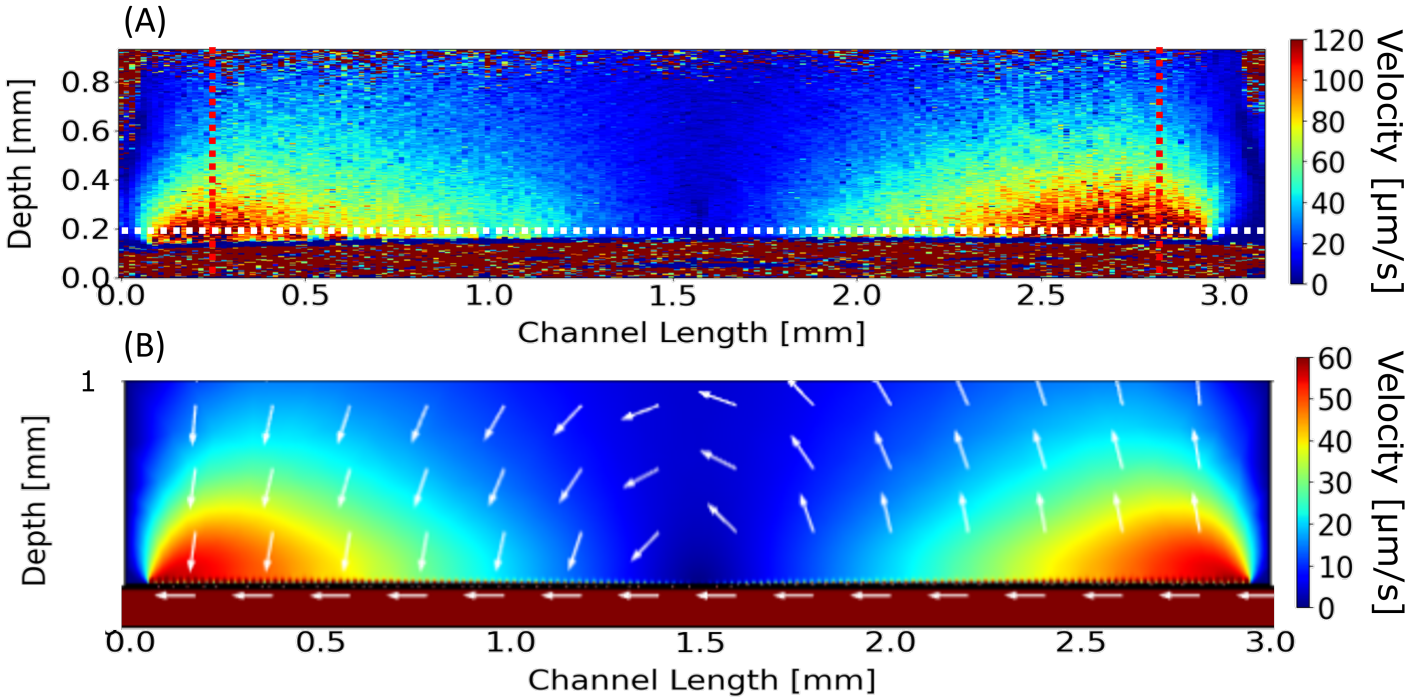

Figure 5.4.: (A) Channel-length B-scan of the OoC displaying the fluid velocity distribution of fluid inside the culture well that enters (from the right of the channel) and exits the culture well (from the left of the channel), via the channel porous membrane, at a pump discharge rate of 40 µl/min. The red dashed lines represent the locations in the OoC that generate the results in Figure 5.5 and the white dashed lines for the results in Figure 5.6. (B) Corresponding COMSOL simulation of the flow in the same system with the inclusion of velocity vectors to visualize the flow direction [64]

Despite the qualitative agreement in the velocity distribution, the experimental velocity values were twofold those calculated in the simulations. The highest velocity of the fluid inside the culture well was at the locations closest to the inlet/outlet. To accurately evaluate the velocity of the fluid at these locations, a cross-section of the 2D data was obtained and the flow in the axial direction (along the dashed red lines) near the outlet (Figure 5.5A) and the inlet (Figure 5.5B) were taken As seen, the velocity was found to be around 115 µm/s and 121 µm/s respectively. In addition, a cross-section of the 2D flow data was taken to show the velocity along the lateral direction (along the white dashed line) near the porous membrane at around 0.2 mm in depth (Figure 5.6A). The plot shows an almost symmetric flow with the first apex representing the outlet, the trough of the plot at the centre representing the centre of the culture well where the flow was the lowest, and finally the second apex representing the inlet. The corresponding simulation of the ideal system is in Figure 5.6B.

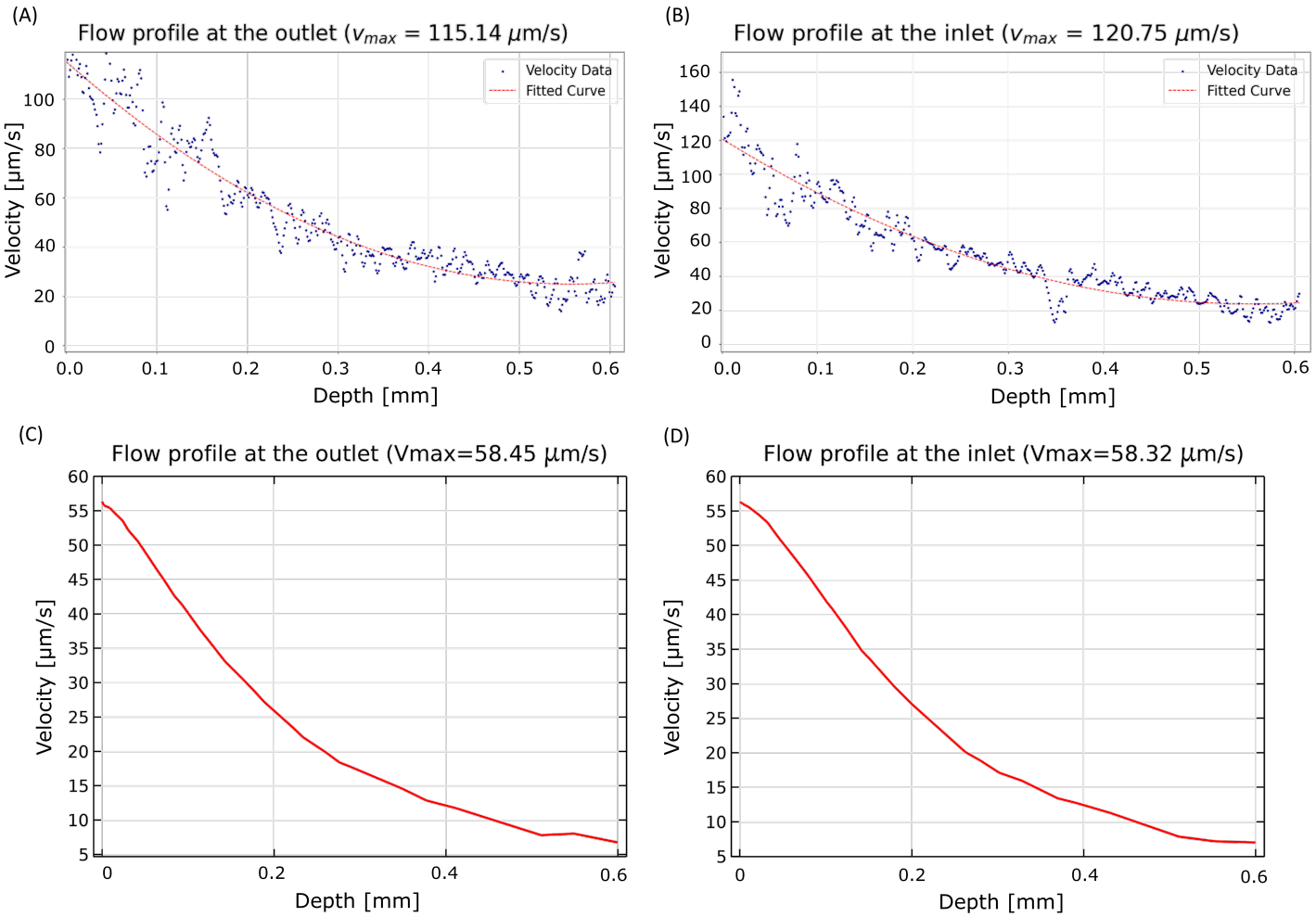

Figure 5.5.: Total velocity along the depth of the culture well near the (A) outlet and (B) inlet of the system showing the maximum velocity at these locations. (C-D) The corresponding simulation results at the same locations [64]

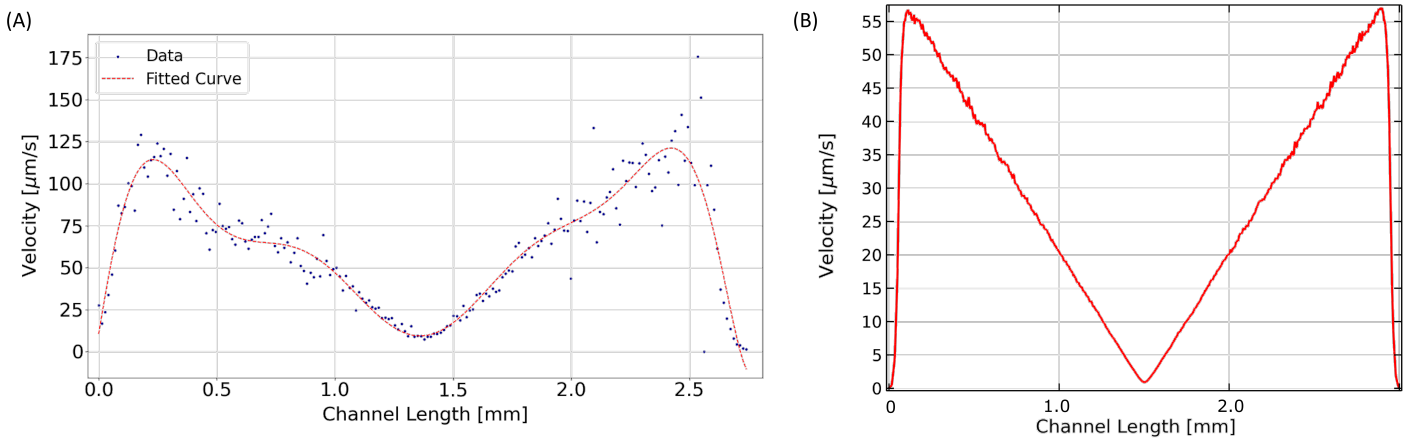

Figure 5.6.: (A) Total velocity along the channel length inside the culture well, close to the porous membrane (0.2 mm into the well). The first apex represents the outlet, followed by the trough of the plot representing the velocity in the centre of the well, and finally, the second apex represents the velocity at the inlet. The fitted curve is strictly for visual aid. (B) The corresponding simulation results at the same location [64]

The results in Figure 5.7 display the fluid velocity distribution inside the culture well that was obtained with cross-sectional B-scans perpendicular to the flow channel. The trends seen in Figure 5.4 were also seen in the cross-sectional results where the flow velocity near the inlet (Figure 5.7A) was slightly higher than the flow velocity near the outlet (Figure 5.7C) and about 10 µm/s at the centre. In addition, looking closely at the microfluidic channel in Figure 5.7B, it is apparent that the physical location of the channel was different than the inlet/outlet measurements. Specifically, the channel cross-section at the centre was protruding into the culture well by about 100 µm compared to the inlet/outlet channel locations. The corresponding simulations (Figure 5.7D-F) show good agreement with the velocity distribution of the experimental measurements but show disagreement with the velocity values, as already discussed in the previous figures.

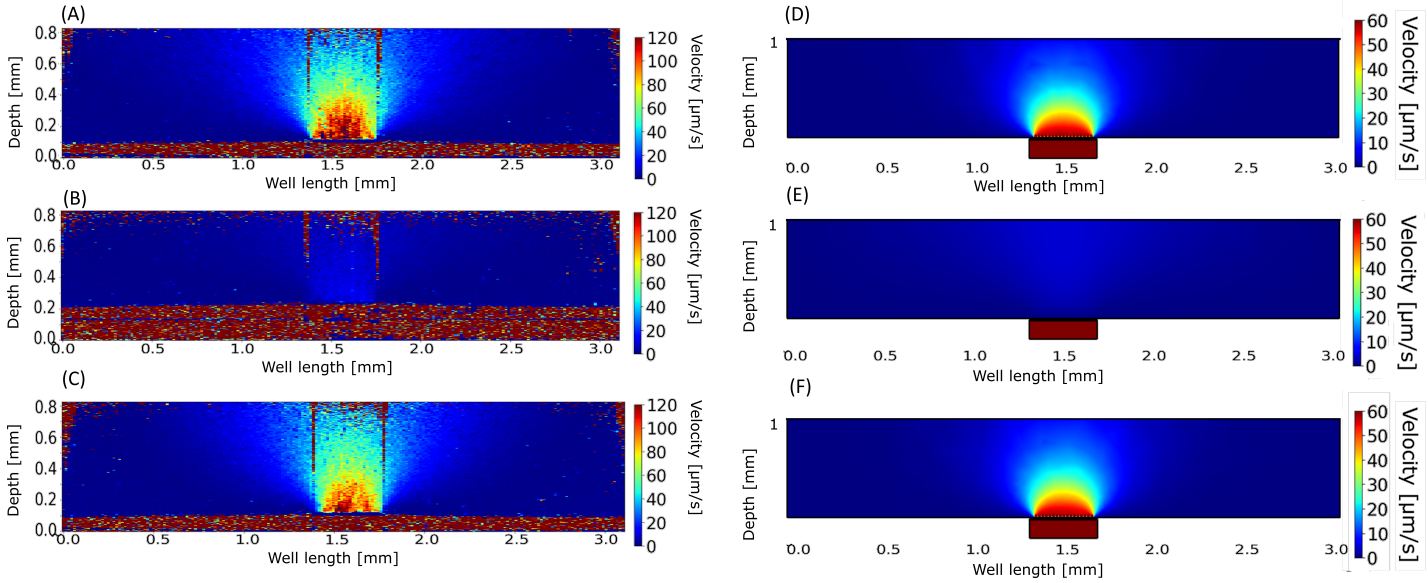

Figure 5.7.: Cross-sectional B-scans of the OoC illustrating the fluid velocity distribution inside the culture well near the (A) inlet, (B) centre, and (C) outlet at a pump discharge rate of 40 µl/min. The dashed white box represents the microfluidic channel. (D-F) The corresponding COMSOL simulations [64]

5.3. OoC applications with cells

The following measurements were conducted in the OoC with the presence of fixed cells to determine the effects of different cell morphologies on the fluid velocities and velocity distributions by replicating the methods that generated the results in the previous sections. The cell-fixed OoCs were prepared by Bi/ond following standard cell seeding protocols. The structural OCT image in Figure 5.8 displays the epithelial cell lining that was initially cultivated in the static culture well and eventually grew through the porous membrane creating restrictions in the lumen of the microfluidic channel. The corresponding measurement of fluid velocity distribution at the same location is visualized in Figure 5.9.

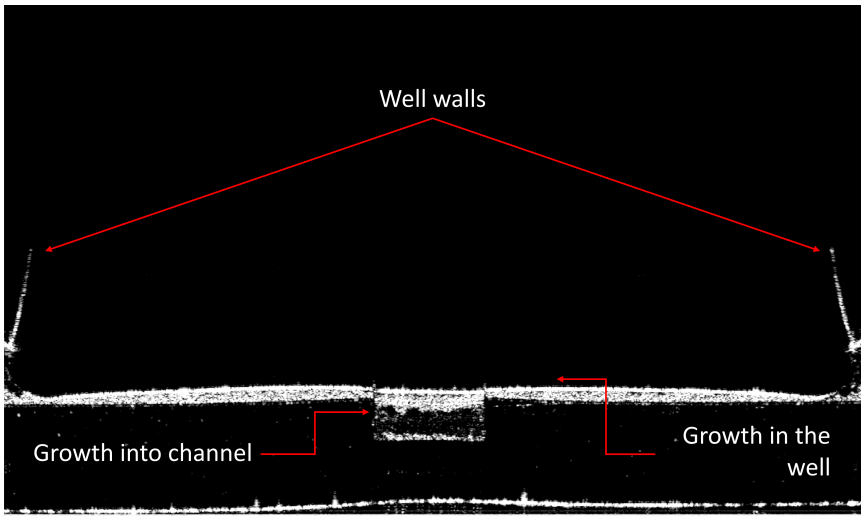

Figure 5.8.: Structural OCT image of the inCHIPit with the presence of fixed epithelial cells that were initially cultured in the culture well but slowly grew into the microfluidic channel through the porous membrane

Figure 5.9C shows the empty channel with the corresponding velocity distribution in Figure 5.9A. Figure 5.9D shows the arbitrary lumen created due to the growth of epithelial cells. The corresponding velocity distribution in Figure 5.9B shows an overall trend where the fluid velocity with the presence of cells is relatively higher when compared to a channel without cells, as shown in Figure 5.9A. Looking at the cell-lined arbitrary lumen of the channel, another trend appears where the regions of the most restricted lumen (e.g. at about 145 µm into the channel width) are the regions with the lowest fluid velocity (about 15 mm/s). Consequently, the fluid flows through regions with the least restriction and results in a relatively higher velocity overall. For clarity, only the epithelial cell culture was presented in this chapter. The remaining conditions with different cell types can be found in Appendix A.

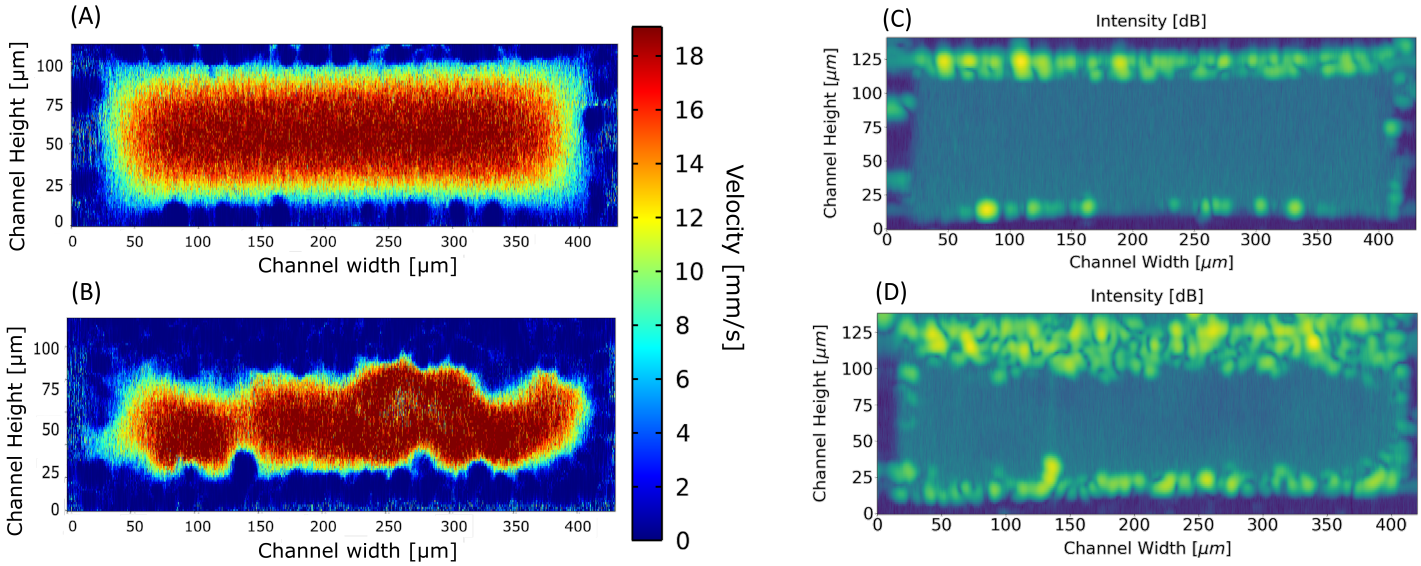

Figure 5.9.: Cross-sectional B-scans that generate the fluid velocity distribution in (A) a channel with no pores and (B) a channel with the presence of epithelial cells protruding from the culture well through the porous membrane. (C-D) are the corresponding structural measurements of the lumen. The pump discharge rate was set to 25 µl/min for all conditions.

6. Discussion

This research began with the simplest measurements of 1D measurements in an OoC without a porous membrane. The absence of a porous membrane allowed the microfluidic channel to act as a simple rectangular flow channel where the theoretically expected flow could simply be calculated, given the dimensions of the channel. In addition, obtaining results with the absence of a porous membrane allowed us to have a ground base level of the flow in the channel. In Figure 5.2, it was shown that the flow along the height of the microfluidic channel formed a parabolic flow profile. The flow profiles showed an increasing deviation from theoretically expected velocity values with increasing pump discharge rates. A small detail in Figure 5.2A explains why this might occur. As mentioned in Chapter 5, with increasing pump discharge rate, the height of the microfluidic channel increased due to the increased pressure difference and the flexibility of the PDMS membrane. Specifically, the height was measured to be 100 µm between the discharge rates of 0-5 µl/min. At discharge rates of 30 µl/min, the height reached 105 µm. Considering geometric scaling laws, a deviation of 5 µm can have significant effects on the flow velocity, especially with a simple rectangular channel. This effect was illustrated in Figure 5.2B where the measured velocity was increasingly lower with increasing discharge rates. In other words, the velocity inside the channel drops with increasing channel height (or volume). On the other hand, the deviation of flow from the theoretical expectation can also be due to an error in the measurement of the Doppler angle. A small error in the Doppler angle measurement can scale with increasing pump discharge rates, creating the same trend that is reflected onto the results. Despite the difficulty in distinguishing whether this trend occurs because of a Doppler angle error or because of the dynamic geometry of the PDMS channel, the author stands with the effect being induced by the dynamic PDMS geometry.

The 2D flow profile in Figure 5.3 captured the inverse relation between flow velocity inside the channel and the channel dimensions. In the 1D measurements, the flow inside the channel decreased with increasing channel volume. In the 2D measurements, the flow inside the channel increased with decreasing channel volume. In the 2D measurements, the height of the channel was measured to be around 90 µm, clearly indicating that the channel lumen was more restricted (compared to a nominal channel height of about 105 µm at 25 µl/min discharge rate for 1D measurements). Therefore, a discrepancy between the flow velocities inside the channel at 25 µl/min occurred. In 1D, the flow velocity at a discharge rate of 25 µl/min was measured to be around 17 mm/s but 23 mm/s in the 2D measurements. In both of these measurements, the only changed variable was the OoC used. It is suspected that this variability in the results was due to the 7.5 µm microfabrication tolerance on the channel height (112.5 µm). Therefore, for the remaining results effort was put to match the simulation dimensions to the experimentally measured dimensions of the OoC.

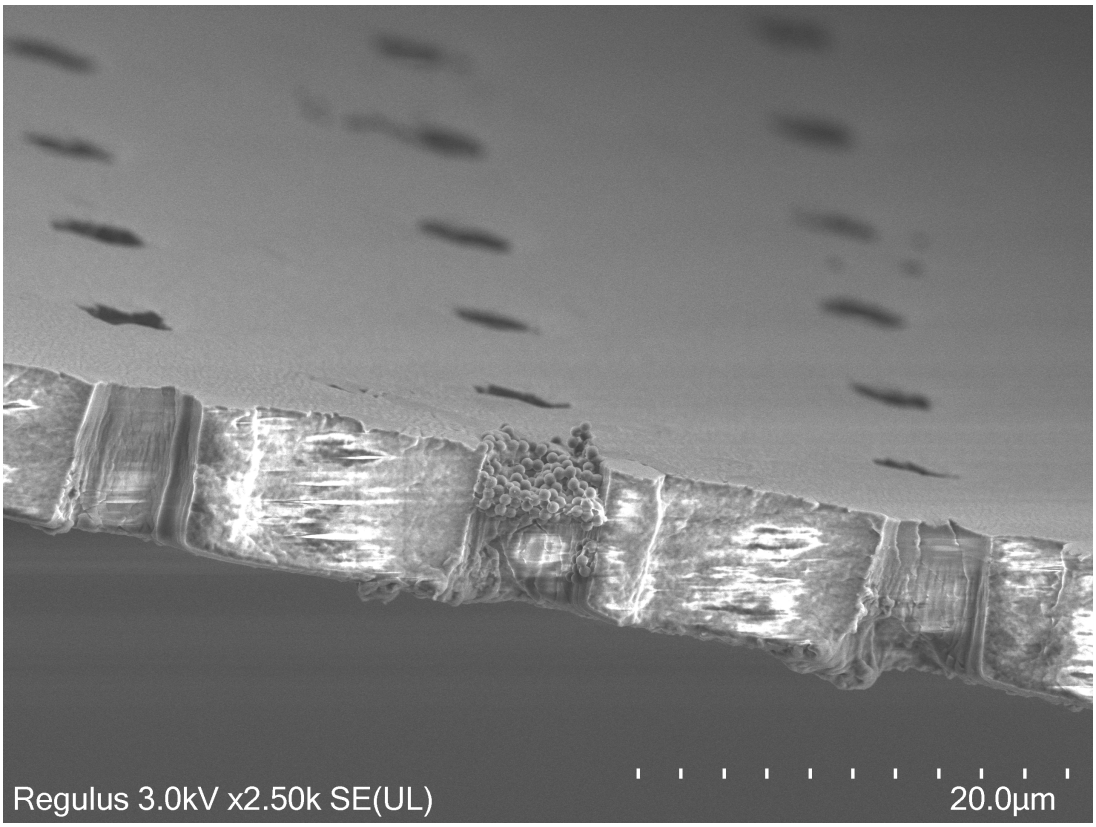

Figure 6.1.: An SEM image showing a sliced porous membrane with a pore clogged with agglomerated polystyrene nanoparticles seen in the center of the image

During this research, moving from an OoC without pores to an OoC with pores was a big challenge. Mainly due to the practical limitation of scattering particles clogging the pores of the system (Figure 6.1). The clogging of the pores created unstable environments within the OoC and made OCT measurements impossible due to the sporadic nature of the clogging. The clogged porous membrane unsteady flow within the system that was visualized with the OCT software in real-time. The flow through the system was rapidly fluctuating due to the clogging of pores and the consequential build-up of pressure that resulted in some pores becoming unclogged and clogged again. After long trials of experimenting, it was deduced that the highly hydrophobic property of PDMS was the main source of clogging and the problem was overcome with surface plasma treatment of the entire OoC. The highly hydrophobic surface of PDMS essentially created such a high repelling force that the 4 µm pores of the system were not accessible by fluid carrying scattering particles. Even particles of 200 nm in diameter would not pass through the pores, either creating clogs or simply rolling over the pores. Therefore, this research highlights a technical limitation of PDMS, independent of the already well-documented PDMS hydrophobicity limitations associated with cell attachment.

In Figure 5.4, the perfusion flow inside the culture well of the OoC was measured. The measurement was taken at a pump discharge rate of 40 µl/min, which translated to a flow velocity of about 120 µm/s near the inlet and about 115 µm/s near the outlet. The main driving force of perfusion flow inside the culture well is due to the Venturi effect [35] created by the porous membrane and microfluidic channel. A 'positive pressure' is created near the inlet, forcing fluid into the well and a 'negative pressure' is created, after the centre point of the channel, that pulls fluid from the culture well back into the channel. In conjunction with the Venturi effect, the velocity of flow being higher near the inlet versus the outlet was suspected due to the pressure

created by the microfluidic pump dropping while moving along the channel, making the regions closest to the inlet have the highest pump pressure, and ultimately the highest flow velocity. The measured velocity distribution in the culture well showed very good qualitative agreement with the corresponding simulation results. However, the measured velocities were two-fold higher than those simulated and the author believes that the mismatch is derived from the limited simulation parameters.

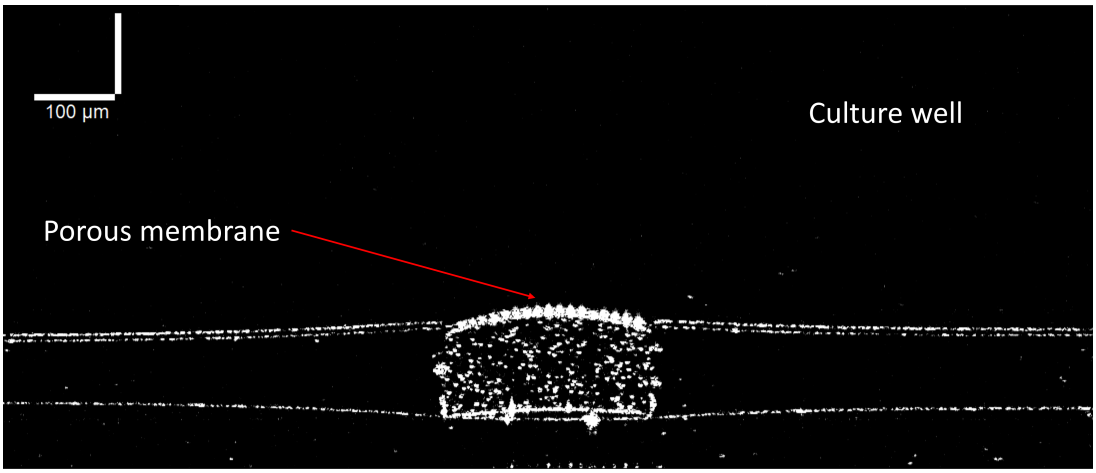

Figure 6.2.: Cross-sectional B-scan of an OoC with a porous membrane that is bulging into the culture well

Firstly, as illustrated with the previous results, the microfluidic channel (along with the porous membrane) is made up of PDMS which is a flexible material. During flow, the system dimensions are dynamic due to the PDMS flexibility and the pressure induced by the pump whereas the simulations assume a static system geometry. The measurements capture the dynamic behaviour of the microfluidic channel. In Figure 5.4A it can be seen that the centre of the channel (about 1.5 mm along the channel length) is at a physically higher location (by 0.1 mm) than the edges of the channel (at 0 and 3 mm along the channel length). This indicates that the centre of the channel is bulging into the culture well by 0.1 mm. This bulging is better seen in Figure 5.7B from a different cross-sectional scanning plane and the bulging of the porous membrane can be visualized in Figure 6.2. For clarity, the bulging observed in Figure 5.7B is different than the one seen in Figure 6.2. In Figure 5.7B, the entire channel is bulging into the culture well, whereas in Figure 6.2 only the porous membrane is bulging into the culture well and not the entire channel. Another consequence of a dynamic microfluidic channel is dynamic pore dimensions. When the channel bulges towards the culture well, the porous membrane is under tension. This would create a gradient pore diameter along the channel length with the pores at the centre (apex of the bulge) having a diameter greater than 4 µm due to the channel being under tension. Finally, the culture lid of the system is designed to partially isolate the culture well from the environment. Partially because the culture lid is not designed to perfectly seal the culture well. As a result, a gradient pressure is present in the culture well whereas the simulation assumes a perfectly sealed, closed-off culture well. The aforementioned multi-factorial physics can have significant effects on the perfusion flow (considering geometrical scaling laws that could have amplified some of these effects) and are thought to be the contributors to the differences in the simulation results.

The final measurements in the OoC were with the presence of fixed cells. The goal was to obtain quantitative information on how the cells influence flow velocities and understand whether OCT

can be compatible with biological applications of OoCs. The ultimate goal is to translate the velocity maps into a shear stress distribution in the channel. The 2D velocity plot in Figure 5.9B shows how the growth of epithelial cells, through the pores and into the channel, affects the flow velocity and velocity distribution. The areas with the most restricted lumen are the areas with the lowest flow rates. Using a parallel resistor model, the fluid always desires to take the path of least resistance. This is seen in the results where the fluid avoids the areas where the lumen is the most restricted but consequently, the velocity of the fluid in non-restricted areas becomes significantly higher. Qualitatively, the areas with the least restricted lumen (highest flow rates) will be the areas that experience the highest shear stresses. The corresponding structural OCT image of the epithelial culture is seen in Figure 5.9D. This image shows the physical locations of the fixed cells inside the channel with the highest cell density being closest to the porous membrane (at about 125 µm along the channel height). This is due to the epithelial cells growing inside the culture well and slowly migrating through the pores, partly into the channel. This measurement ultimately shows that with time-lapsed acquisition periods, the cell monolayer growth can be quantified. To illustrate the potential OCT measurements carry in biological OoC evaluations, an experiment was run with the presence of a liver sample inside the culture well of the system. The aim was for the liver sample to represent an organoid that would be cultured inside the well. Due to lack of time, no quantitative information was drawn from the measurements and only a structural OCT measurement was obtained, along with qualitative videos. The image can be seen in Figure 6.3.

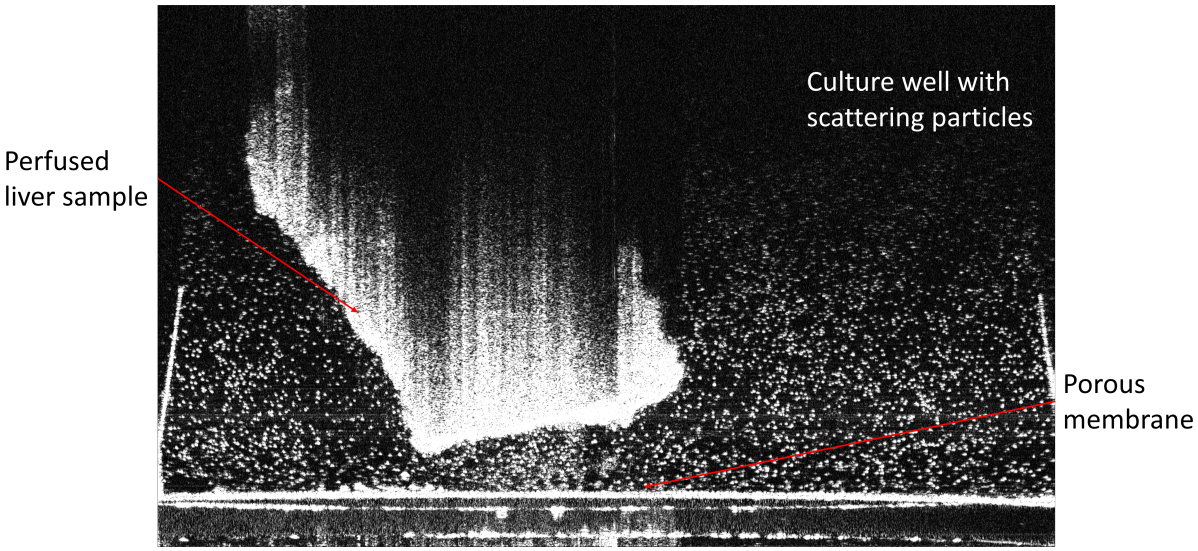

Figure 6.3.: Channel length B-scan of an OoC with liver sample placed inside the culture well

Finally, an extensive literature study was conducted as part of this research. The literature showed that techniques allowing the real-time quantitative measurement of flow rates inside OoCs exist and have been applied to microfluidic OoCs in the past, with each technique having its advantages and limitations. Some of these limitations can be alleviated by combining several techniques, just like this research, in conjunction with the OoC geometry but it is worth recognizing that the limitations go beyond those that come from the measurement techniques alone. Despite the nano-scale precision of the microfabrication processes that produce OoCs, variability between each chip is a known problem and still exists. This poses an extra challenge for generating repeatable, quantitative flow data. Despite the well documented applications of techniques such as particle image velocimetry, particle streak velocimetry, and Doppler-OCT, all these techniques in the literature were applied to OoC systems with well defined, relatively simple geome-

tries that produced flow patterns that could easily be predicted through theoretical calculations and modelled with CFD models. The OoC systems studied in the literature did not encompass the vast variety of microarchitecture in microfluidic OoCs that exist to facilitate features like passive valves, gravity-driven rocker-induced flows, flow through permeable and flexible membranes, microdroplet formation, concentration gradients and more. Therefore, in contrast with the literature on this topic, the results of this research show that quantitative measurement of complex flow patterns inside microfluidic OoCs using OCT is possible at high resolutions and in real-time. The author believes that this research was the stepping stone to demonstrate the versatility of OCT and the potential it carries on bringing new data to OoCs and OoC applications. Nevertheless, the process will be non-trivial and multidisciplinary involving fluid mechanics, materials science, microfluidics, physics, tissue engineering and microfabrication processes.

7. Conclusion & Future Recommendations

During this research, the capability of OCT techniques to obtain quantitative flow data in a microfluidic OoC was questioned. Structural OCT images of the OoC were obtained in real-time and the information was used to perform system inspections that helped define system geometries and validate microfabrication outcomes. In addition, structural information was also obtained while the OoC was being operated (during active flow) to gain insight into how the internal microstructure deviated from static conditions (no flow). Parallel to the structural information, the flow velocity in different regions of the OoC was quantitatively evaluated. This data helped us understand the velocity distribution throughout the system and define important regions that are biologically relevant. In addition, the effects of surface plasma treatment on the OoC functionality were qualitatively observed and the effects of PDMS hydrophobicity on the technical aspects of the OoC was highlighted. The flow results also demonstrated the deviation of real system behaviour from the limiting assumptions made in the corresponding simulation models. Finally, the methods were repeated with the presence of cultured cells (fixed) to demonstrate OCT compatibility with the biological applications OoCs are designed for. Overall, the results are positive and prove that quantitative measurements of flow inside a microfluidic OoC model are possible.

Despite the positive results, the techniques applied in the research can be improved to generate more quantitative results. Specifically, the total velocity distribution in the system was determined through the varying OCT techniques. An improvement would be to measure different vector components (axial and transverse) of the velocity. Measuring the velocity vector components would allow us to get information on the flow directionality throughout the system (i.e. 2D vector plots). To do this, the angle (θ) of the flow vectors needs to be determined and can be quantitatively determined with 1D M-scans. Independent of the vector components, the quantitative measurement of the flow angle would be an improvement within itself. In addition, the ultimate purpose of OoCs is to facilitate in-vitro models. Therefore, quantitative flow measurements in real-time, during the presence of cells in the system are desired. To achieve this, the scattering particles need to be optimized to ensure biocompatibility and avoid cytotoxicity, and the methods need to be optimized to account for newly introduced technical difficulties (e.g. increased signal polluting internal reflections due to biological samples in the OoC).

A. More Results

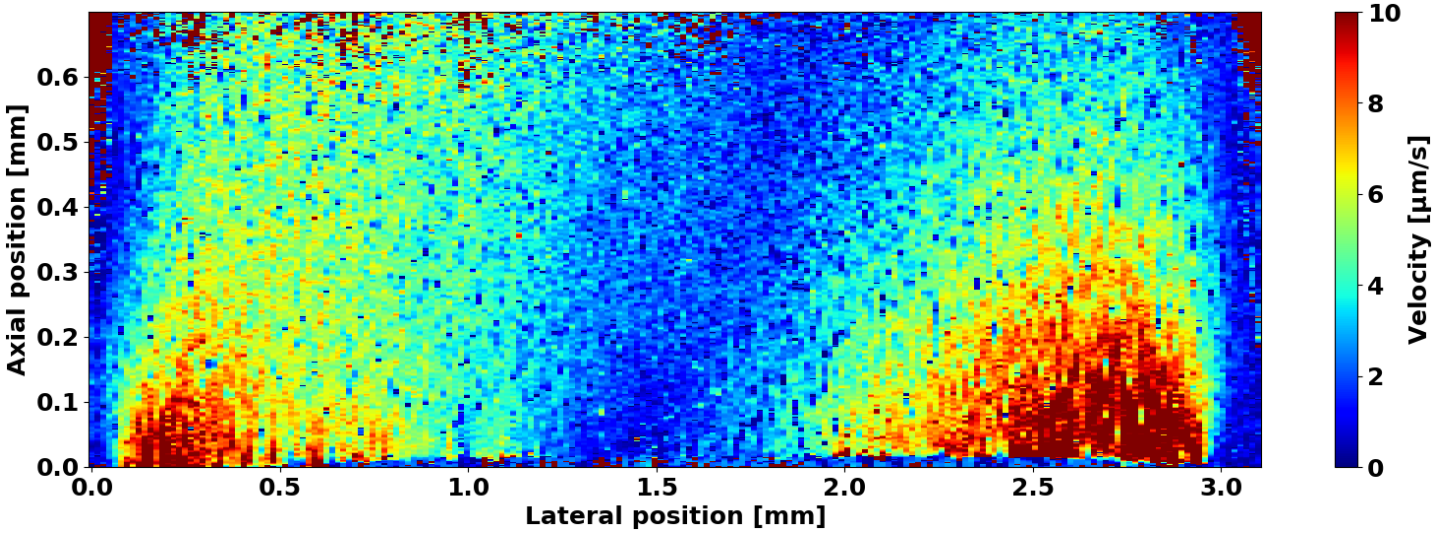

Figure A.1.: Fluid velocity distribution of the perfusion flow with a pump discharge rate of 5 µl/min. The microfluidic channel is not shown

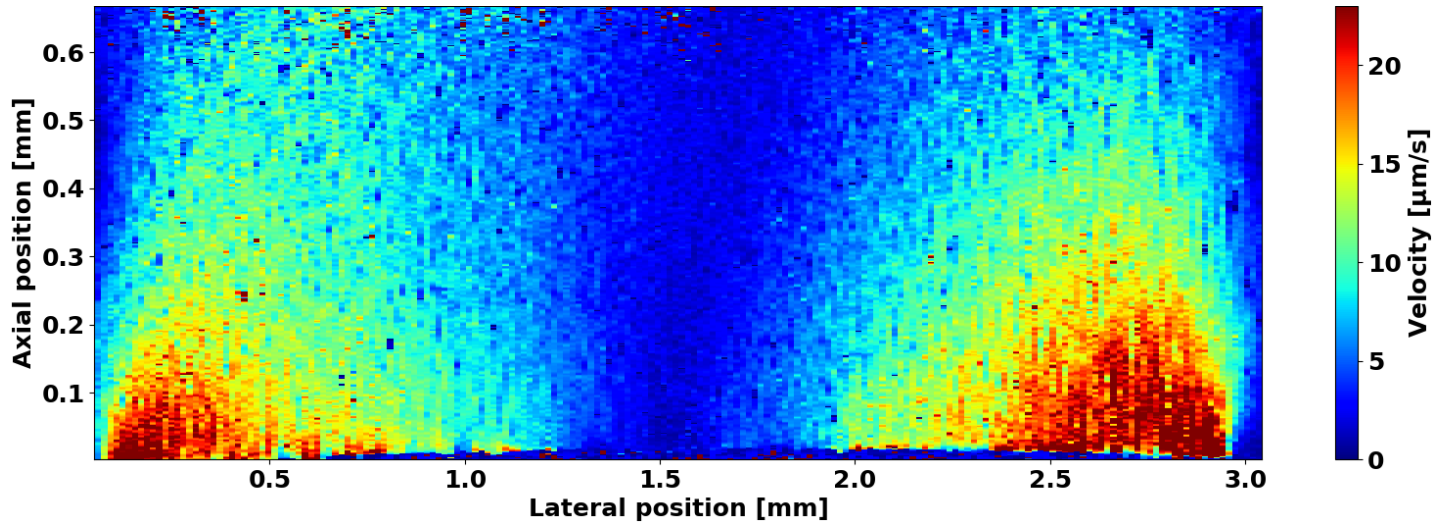

Figure A.2.: Fluid velocity distribution of the perfusion flow with a pump discharge rate of 10 µl/min. The microfluidic channel is not shown

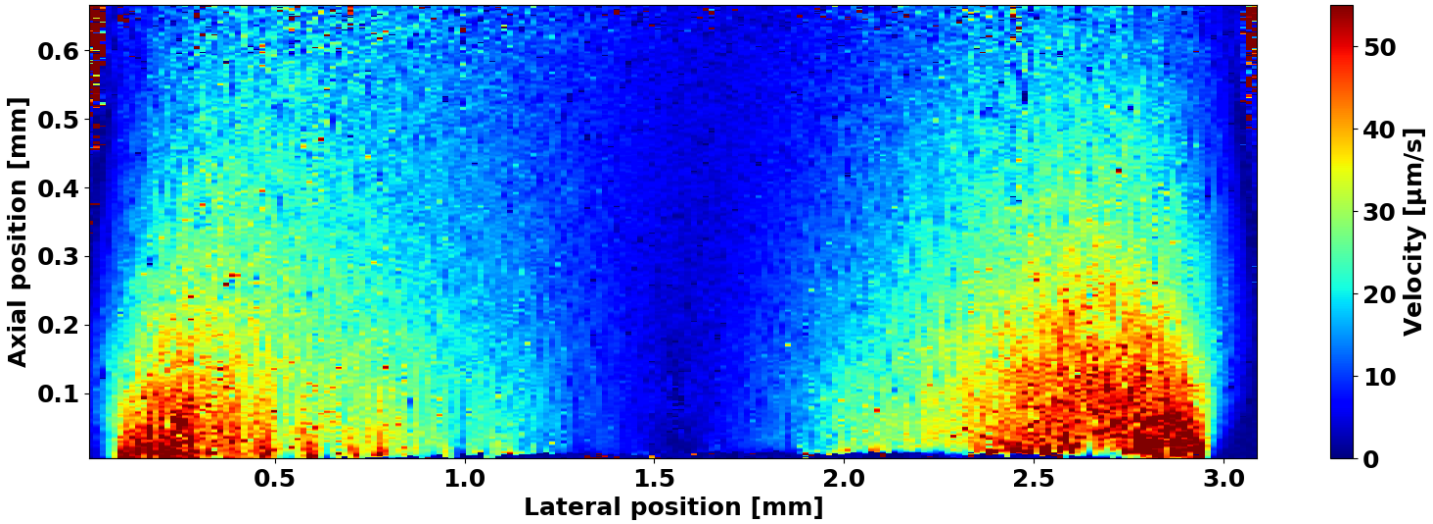

Figure A.3.: Fluid velocity distribution of the perfusion flow with a pump discharge rate of 25 µl/min. The microfluidic channel is not shown

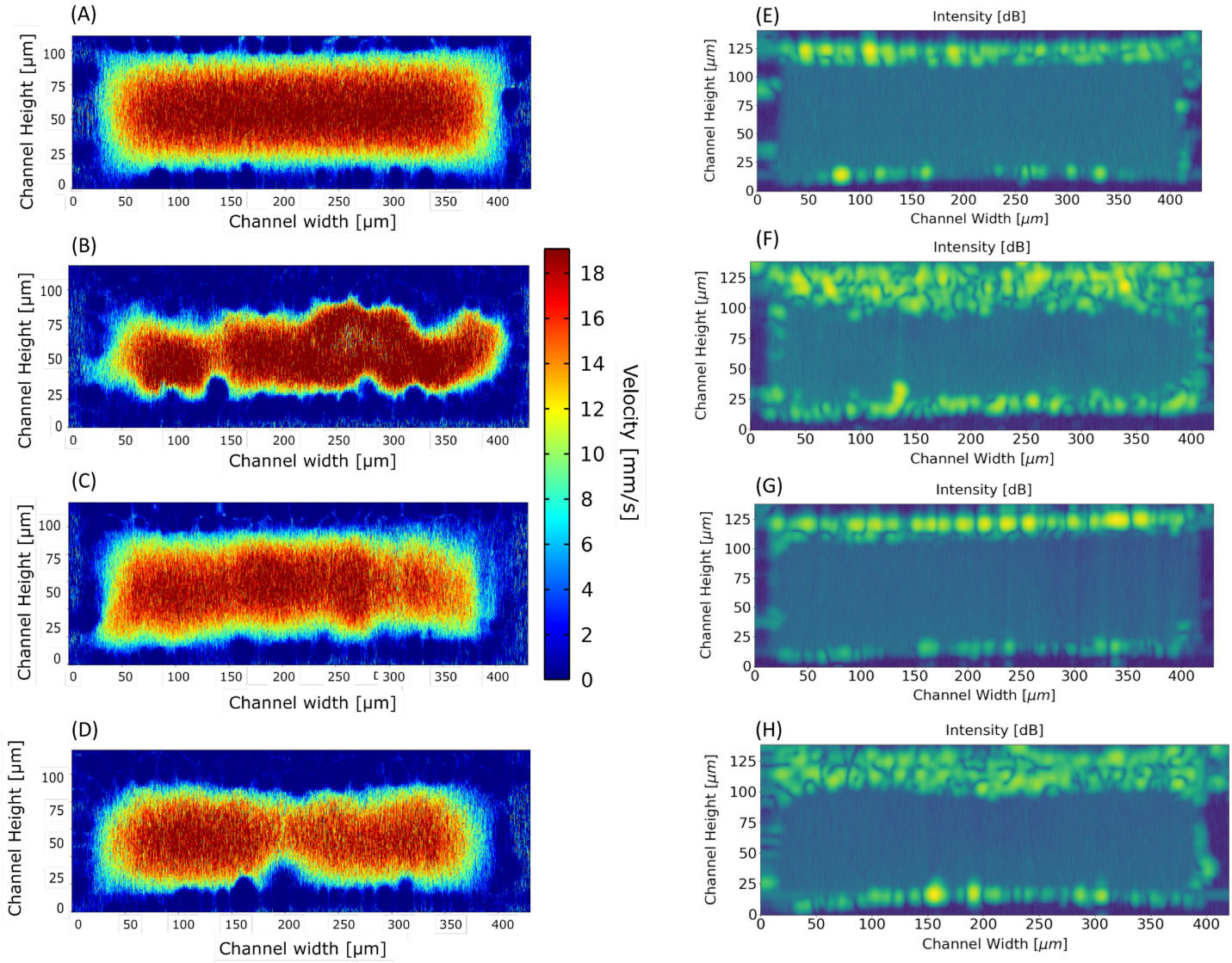

Figure A.4.: Cross-sectional B-scans that generate the fluid velocity distribution in (A) an empty channel, (B) a channel with the presence of epithelial cells protruding from the culture well through the porous membrane, (C) a channel with endothelial cell monolayer lining the perimeter of the channel, and (D) a co-culture of the epithelial and endothelial cells. (E-H) are the corresponding structural measurements of the channel. The pump discharge rate was set to 25 µl/min for all conditions

Bibliography

[1] Akther, F., Yakob, S. B., Nguyen, N.-T., and Ta, H. T. (2020). Surface modification techniques for endothelial cell seeding in pdms microfluidic devices. *Biosensors*, 10(11).

[2] An, Y., Jin, T., Zhang, F., and He, P. (2019). Electric cell-substrate impedance sensing (ecis) for profiling cytotoxicity of cigarette smoke. *Journal of Electroanalytical Chemistry*, 834:180–186.

[3] Aydogmus, H., Hu, M., Ivancevic, L., Frimat, J.-P., van den Maagdenberg, A. M. J. M., Sarro, P. M., and Mastrangeli, M. (2023). An organ-on-chip device with integrated charge sensors and recording microelectrodes. *Scientific Reports*, 13(1):8062.

[4] Bavli, D., Prill, S., Ezra, E., Levy, G., Cohen, M., Vinken, M., Vanfleteren, J., Jaeger, M., and Nahmias, Y. (2016). Real-time monitoring of metabolic function in liver-on-chip microdevices tracks the dynamics of mitochondrial dysfunction. *Proceedings of the National Academy of Sciences*, 113(16):E2231–E2240.

[5] Beißner, N., Lorenz, T., and Reichl, S. (2016). *Organ on Chip*, pages 299–339. Springer International Publishing, Cham.

[6] Brezinski, M. E., Tearney, G. J., Bouma, B., Boppart, S. A., Pitris, C., Southern, J. F., and Fujimoto, J. G. (1998). Optical biopsy with optical coherence tomography. *Ann N Y Acad Sci*, 838:68–74.

[7] Brillouin, L. (1914). Light diffusion by a homogeneous transparent body. *Cr Hebd Acad Sci*, 158:1331–1334.

[8] Bryant, F. (1958). Snell's law of refraction. *Physics Bulletin*, 9(12):317.

[9] Buchanan, B. C. and Yoon, J.-Y. (2022). Microscopic imaging methods for Organ-on-a-Chip platforms. *Micromachines (Basel)*, 13(2).

[10] Busek, M., Aizenshtadt, A., Koch, T., Frank, A., Delon, L., Martinez, M. A., Golovin, A., Dumas, C., Stokowiec, J., Gruenzner, S., Melum, E., and Krauss, S. (2023). Pump-less, recirculating organ-on-a-chip (rooc) platform. *Lab Chip*, 23:591–608.

[11] Busek, M., Polk, C., Albrecht, T., Marx, U., König, J., and Sonntag, F. (2012). Automated micro-piv measurement in lab-on-a-chip systems. *Biomedical Engineering / Biomedizinische Technik*, 57(SI-1-Track-E):927–930.

[12] Cannady, E., Katyayan, K., and Patel, N. (2022). Chapter 3 - adme principles in small molecule drug discovery and development: An industrial perspective. In Haschek, W. M., Rousseaux, C. G., Wallig, M. A., and Bolon, B., editors, *Haschek and Rousseaux's Handbook of Toxicologic Pathology (Fourth Edition)*, pages 51–76. Academic Press, fourth edition edition.

[13] Cheishvili, K. and Kalkman, J. (2022). Scanning dynamic light scattering optical coherence tomography for measurement of high omnidirectional flow velocities. *Opt. Express*, 30(13):23382–23397.

[14] Cheishvili, K. and Kalkman, J. (2023a). Sub-diffusion flow velocimetry with number fluctuation optical coherence tomography. *Opt. Express*, 31(3):3755–3773.

[15] Cheishvili, K. and Kalkman, J. (2023b). Sub-diffusion flow velocimetry with number fluctuation optical coherence tomography, https://doi.org/10.5281/zenodo.6606471.

[16] Chen, Z., Milner, T. E., Srinivas, S., Wang, X., Malekafzali, A., van Gemert, M. J. C., and Nelson, J. S. (1997). Noninvasive imaging of in vivo blood flow velocity using optical doppler tomography. *Opt. Lett.*, 22(14):1119–1121.

[17] Chen, Z., Zhao, Y., and M.D., J. S. N. (2001). Phase-resolved optical coherence tomography and optical Doppler tomography: technology and applications. In Tuchin, V. V., editor, *Saratov Fall Meeting 2000: Optical Technologies in Biophysics and Medicine II*, volume 4241, pages 182 – 185. International Society for Optics and Photonics, SPIE.

[18] Cho, S., Lee, S., and Ahn, S. I. (2023). Design and engineering of organ-on-a-chip. *Biomedical Engineering Letters*, 13(2):97–109.

[19] Clarke, G. A., Hartse, B. X., Niaraki Asli, A. E., Taghavimehr, M., Hashemi, N., Abbasi Shirsavar, M., Montazami, R., Alimoradi, N., Nasirian, V., Ouedraogo, L. J., and Hashemi, N. N. (2021). Advancement of sensor integrated organ-on-chip devices. *Sensors*, 21(4).

[20] Currie, G. P., Lee, D. K., and Lipworth, B. J. (2006). Long-acting β2-agonists in asthma. *Drug Safety*, 29(8):647–656.

[21] da Silva, R. G. L. and Blasimme, A. (2023). Organ chip research in europe: players, initiatives, and policies. *Frontiers in Bioengineering and Biotechnology*, 11.

[22] Daley, M. C., Bonzanni, M., MacKenzie, A. M., Kaplan, D. L., and Black, 3rd, L. D. (2020). The effects of membrane potential and extracellular matrix composition on vascular differentiation of cardiac progenitor cells. *Biochem Biophys Res Commun*, 530(1):240–245.

[23] de Carlo, T. E., Romano, A., Waheed, N. K., and Duker, J. S. (2015). A review of optical coherence tomography angiography (OCTA). *International Journal of Retina and Vitreous*, 1(1):5.

[24] DePond, P. J., Guss, G., Ly, S., Calta, N. P., Deane, D., Khairallah, S., and Matthews, M. J. (2018). In situ measurements of layer roughness during laser powder bed fusion additive manufacturing using low coherence scanning interferometry. *Materials & Design*, 154:347–359.

[25] Drexler, W. and Fujimoto, J. G. (2008). *Optical coherence tomography: technology and applications*. Springer Science & Business Media.

[26] Driver, R. and Mishra, S. (2023). Organ-on-a-chip technology: An in-depth review of recent advancements and future of whole body-on-chip. *BioChip Journal*, 17(1):1–23.

[27] Du, Y., Khandekar, G., Llewellyn, J., Polacheck, W., Chen, C. S., and Wells, R. G. (2020). A bile duct-on-a-chip with organ-level functions. *Hepatology*, 71(4):1350–1363.

[28] Einstein, A. (1905). Über einen die erzeugung und verwandlung des lichtes betreffenden heuristischen gesichtspunkt. *Annalen der Physik*, 322(6):132–148.

[29] et al., M. U. (2016). Biology-inspired microphysiological system approaches to solve the prediction dilemma of substance testing. *ALTEX*, 33(3):272–321.

[30] Fercher, A. F., Mengedoht, K., and Werner, W. (1988). Eye-length measurement by interferometry with partially coherent light. *Opt. Lett.*, 13(3):186–188.

[31] Foord, R., Jakeman, E., Oliver, C. J., Pike, E. R., Blagrove, R. J., Wood, E., and Peacocke, A. R. (1970). Determination of diffusion coefficients of haemocyanin at low concentration by intensity fluctuation spectroscopy of scattered laser light. *Nature*, 227(5255):242–245.

[32] Fuchs, S., Johansson, S., Tjell, A. Ø., Werr, G., Mayr, T., and Tenje, M. (2021). In-Line analysis of Organ-on-Chip systems with sensors: Integration, fabrication, challenges, and potential. *ACS Biomater. Sci. Eng.*, 7(7):2926–2948.

[33] Gabriele, M. L., Wollstein, G., Ishikawa, H., Kagemann, L., Xu, J., Folio, L. S., and Schuman, J. S. (2011). Optical coherence tomography: history, current status, and laboratory work. *Invest Ophthalmol Vis Sci*, 52(5):2425–2436.

[34] Gaio, N. (2012). *Organ-on-Silicon*. PhD thesis, Delft University of Technology.

[35] Gallitto, A. A., Zingales, R., Battaglia, O. R., and Fazio, C. (2021). An approach to the venturi effect by historical instruments. *Physics Education*, 56(2):025007.

[36] Goldrick, C., Guri, I., Herrera-Oropeza, G., O'Brien-Gore, C., Roy, E., Wojtynska, M., and Spagnoli, F. M. (2023). 3D multicellular systems in disease modelling: From organoids to organ-on-chip. *Front Cell Dev Biol*, 11:1083175.

[37] Han, W. M., Jang, Y. C., and García, A. J. (2020). 2.1.5 - the extracellular matrix and cell–biomaterial interactions. In Wagner, W. R., Sakiyama-Elbert, S. E., Zhang, G., and Yaszemski, M. J., editors, *Biomaterials Science (Fourth Edition)*, pages 701–715. Academic Press, fourth edition edition.

[38] Huh, D., Matthews, B. D., Mammoto, A., Montoya-Zavala, M., Hsin, H. Y., and Ingber, D. E. (2010a). Reconstituting organ-level lung functions on a chip. *Science*, 328(5986):1662–1668.

[39] Huh, D., Matthews, B. D., Mammoto, A., Montoya-Zavala, M., Hsin, H. Y., and Ingber, D. E. (2010b). Reconstituting organ-level lung functions on a chip. *Science*, 328(5986):1662–1668.

[40] Izatt, J. A., Kulkarni, M. D., Yazdanfar, S., Barton, J. K., and Welch, A. J. (1997). In vivo bidirectional color doppler flow imaging of picoliter blood volumes using optical coherence tomography. *Opt. Lett.*, 22(18):1439–1441.

[41] Jalili-Firoozinezhad, S., Miranda, C. C., and Cabral, J. M. (2021). Modeling the human body on microfluidic chips. *Trends in Biotechnology*, 39(8):838–852. Special Issue: Microphysiological Systems.

[42] Kalkman, J. (2017). Fourier-Domain optical coherence tomography signal analysis and numerical modeling. *International Journal of Optics*, 2017:9586067.

[43] Kimura, H., Ikeda, T., Nakayama, H., Sakai, Y., and Fujii, T. (2015). An on-chip small intestine–liver model for pharmacokinetic studies. *Journal of Laboratory Automation*, 20(3):265–273. PMID: 25385717.

[44] Koch, E., Walther, J., and Cuevas, M. (2009). Limits of fourier domain doppler-oct at high velocities. *Sensors and Actuators A: Physical*, 156(1):8–13. EUROSENSORS XXII, 2008.

[45] Kutluk, H., Bastounis, E. E., and Constantinou, I. (2023). Integration of extracellular matrices into organ-on-chip systems. *Advanced Healthcare Materials*, n/a(n/a):2203256.

[46] Lauri, J., Czajkowski, J., Myllylä, R., and Fabritius, T. (2015). Measuring flow dynamics in a microfluidic chip using optical coherence tomography with 1µm axial resolution. *Flow Measurement and Instrumentation*, 43:1–5.

[47] Lee, J., Wu, W., Jiang, J. Y., Zhu, B., and Boas, D. A. (2012). Dynamic light scattering optical coherence tomography. *Opt. Express*, 20(20):22262–22277.

[48] Liu, G. and Chen, Z. (2013). Advances in doppler OCT. *Chin Opt Lett*, 11(1):11702.

[49] Ma, C., Peng, Y., Li, H., and Chen, W. (2021). Organ-on-a-chip: A new paradigm for drug development. *Trends in Pharmacological Sciences*, 42(2):119–133.

[50] Malm, A. (2015). *OCT Velocimetry and X-ray Scattering Rheology of Complex Fluids*. PhD thesis, University of Manchester.

[51] Marx, U., Akabane, T., Andersson, T. B., Baker, E., Beilmann, M., Beken, S., Brendler-Schwaab, S., Cirit, M., David, R., Dehne, E.-M., Durieux, I., Ewart, L., Fitzpatrick, S. C., Frey, O., Fuchs, F., Griffith, L. G., Hamilton, G. A., Hartung, T., Hoeng, J., Hogberg, H., Hughes, D. J., Ingber, D. E., Iskandar, A., Kanamori, T., Kojima, H., Kuehnl, J., Leist, M., Li, B., Loskill, P., Mendrick, D. L., Neumann, T., Pallocca, G., Rusyn, I., Smirnova, L., Steger-Hartmann, T., Tagle, D. A., Tonevitsky, A., Tsyb, S., Trapecar, M., Van de Water, B., Van den Eijnden-van Raaij, J., Vulto, P., Watanabe, K., Wolf, A., Zhou, X., and Roth, A. (2020). Biology-inspired microphysiological systems to advance patient benefit and animal welfare in drug development. *ALTEX*, 37(3):365–394.

[52] Mastrangeli, M., Millet, S., Mummery, C., Loskill, P., Braeken, D., Eberle, W., Cipriano, M., Fernandez, L., Graef, M., Gidrol, X., Picollet-D'Hahan, N., van Meer, B., Ochoa, I., Schutte, M., and van den Eijnden-van Raaij, J. (2019a). Building blocks for a european organ-on-chip roadmap. *ALTEX - Alternatives to animal experimentation*, 36(3):481–492.

[53] Mastrangeli, M., Millet, S., Orchid Partners, The, and Van den Eijnden-van Raaij, J. (2019b). Organ-on-chip in development: Towards a roadmap for organs-on-chip. *ALTEX*, 36(4):650–668.

[54] Mastrangeli, M. and van den Eijnden-van Raaij, J. (2021). Organs-on-chip: The way forward. *Stem Cell Reports*, 16(9):2037–2043.

[55] Morales, I. A., Boghdady, C.-M., Campbell, B. E., and Moraes, C. (2022). Integrating mechanical sensor readouts into organ-on-a-chip platforms. *Frontiers in Bioengineering and Biotechnology*, 10.

[56] Mousavi Shaegh, S. A., De Ferrari, F., Zhang, Y. S., Nabavinia, M., Binth Mohammad, N., Ryan, J., Pourmand, A., Laukaitis, E., Banan Sadeghian, R., Nadhman, A., Shin, S. R., Nezhad, A. S., Khademhosseini, A., and Dokmeci, M. R. (2016). A microfluidic optical platform for real-time monitoring of pH and oxygen in microfluidic bioreactors and organ-on-chip devices. *Biomicrofluidics*, 10(4):044111.

[57] Mukherjee, D. and Topol, E. J. (2002). Pharmacogenomics in cardiovascular diseases. *Progress in Cardiovascular Diseases*, 44(6):479–498. Unstable Plaque, Part II.

[58] Nelson, J. S., Kelly, K. M., Zhao, Y., and Chen, Z. (2001). Imaging Blood Flow in Human Port-wine Stain In Situ and in Real Time Using Optical Doppler Tomography. *Archives of Dermatology*, 137(6):741–744.

[59] no author (2023). Yole group website - https://www.yolegroup.com.

[60] Orr, A. W., Helmke, B. P., Blackman, B. R., and Schwartz, M. A. (2006). Mechanisms of mechanotransduction. *Developmental Cell*, 10(1):11–20.

[61] Osório, L. A., Silva, E., and Mackay, R. E. (2021). A review of biomaterials and scaffold fabrication for organ-on-a-chip (ooac) systems. *Bioengineering*, 8(8).

[62] Park, J., Kim, K. B., Lee, J., Kim, H. C., and Huh, D. (2012). Organomimetic microsystems technologies. *Biomedical Engineering Letters*, 2(2):88–94.

[63] Pecora, R. (2004). Doppler Shifts in Light Scattering from Pure Liquids and Polymer Solutions. *The Journal of Chemical Physics*, 40(6):1604–1614.

[64] Quirós-Solano, W. (2023). Computer Fluid Dynamic Models - COMSOL.

[65] Reyes, D. R., van Heeren, H., Guha, S., Herbertson, L., Tzannis, A. P., Ducrée, J., Bissig, H., and Becker, H. (2021). Accelerating innovation and commercialization through standardization of microfluidic-based medical devices. *Lab Chip*, 21:9–21.

[66] Safai, E. (2020). Evaluation of organ-on-chip microfluidic flows using optical coherence tomography. Master's thesis, Delft University of Technology.

[67] Song, G. and Harding, K. (2012). OCT for industrial applications. In Harding, K. G., Huang, P. S., and Yoshizawa, T., editors, *Optical Metrology and Inspection for Industrial Applications II*, volume 8563, page 85630N. International Society for Optics and Photonics, SPIE.

[68] Stetefeld, J., McKenna, S. A., and Patel, T. R. (2016). Dynamic light scattering: a practical guide and applications in biomedical sciences. *Biophysical Reviews*, 8(4):409–427.

[69] Strutt, J. (1871a). Lviii. on the scattering of light by small particles. *The London, Edinburgh, and Dublin Philosophical Magazine and Journal of Science*, 41(275):447–454.

[70] Strutt, J. (1871b). Xxxvi. on the light from the sky, its polarization and colour. *The London, Edinburgh, and Dublin Philosophical Magazine and Journal of Science*, 41(273):274–279.

[71] Taylor, A. M., Dieterich, D. C., Ito, H. T., Kim, S. A., and Schuman, E. M. (2010). Microfluidic local perfusion chambers for the visualization and manipulation of synapses. *Neuron*, 66(1):57–68.

[72] Turner, A., Karube, I., and Wilson, G. S. (1987). Biosensors : Fundamentals and applications.

[73] Tyndall, J. (1869). Iv. on the blue colour of the sky, the polarization of skylight, and on the polarization of light by cloudy matter generally. *Proceedings of the Royal Society of London*, 17:223–233.

[74] Vatine, G. D., Barrile, R., Workman, M. J., Sances, S., Barriga, B. K., Rahnama, M., Barthakur, S., Kasendra, M., Lucchesi, C., Kerns, J., Wen, N., Spivia, W. R., Chen, Z., Van Eyk, J., and Svendsen, C. N. (2019). Human ipsc-derived blood-brain barrier chips enable disease modeling and personalized medicine applications. *Cell Stem Cell*, 24(6):995–1005.e6.

[75] Vrbanac, J. and Slauter, R. (2017). Chapter 3 - adme in drug discovery. In Faqi, A. S., editor, *A Comprehensive Guide to Toxicology in Nonclinical Drug Development (Second Edition)*, pages 39–67. Academic Press, Boston, second edition edition.

[76] Welzel, J. (2001). Optical coherence tomography in dermatology: a review. *Skin Research and Technology*, 7(1):1–9.

[77] Wen, J. H., Vincent, L. G., Fuhrmann, A., Choi, Y. S., Hribar, K. C., Taylor-Weiner, H., Chen, S., and Engler, A. J. (2014). Interplay of matrix stiffness and protein tethering in stem cell differentiation. *Nat Mater*, 13(10):979–987.

[78] White, R. (2017). 4.01 - role of adme/pk in drug discovery, safety assessment, and clinical development. In Chackalamannil, S., Rotella, D., and Ward, S. E., editors, *Comprehensive Medicinal Chemistry III*, pages 1–33. Elsevier, Oxford.

[79] Wikswo, J. P. (2014). The relevance and potential roles of microphysiological systems in biology and medicine. *Experimental biology and medicine*, 239(9):1061–1072.

[80] Xi, C., Marks, D. L., Parikh, D. S., Raskin, L., and Boppart, S. A. (2004). Structural and functional imaging of 3d microfluidic mixers using optical coherence tomography. *Proceedings of the National Academy of Sciences*, 101(20):7516–7521.

[81] Zarifi, M. H., Sadabadi, H., Hejazi, S. H., Daneshmand, M., and Sanati-Nezhad, A. (2018). Noncontact and nonintrusive Microwave-Microfluidic flow sensor for energy and biomedical engineering. *Scientific Reports*, 8(1):139.

[82] Zheng, F., Fu, F., Cheng, Y., Wang, C., Zhao, Y., and Gu, Z. (2016). Organ-on-a-chip systems: Microengineering to biomimic living systems. *Small*, 12(17):2253–2282.

[83] Zhou, J., Ellis, A. V., and Voelcker, N. H. (2010). Recent developments in pdms surface modification for microfluidic devices. *ELECTROPHORESIS*, 31(1):2–16.